Available online at www.sciencedirect.com

SciVerse ScienceDirect

Ceramics International 39 (2013) 649–672

CERAMICS INTERNATIONAL

www.elsevier.com/locate/ceramint

Erosion of atmospheric plasma sprayed rare earth oxide coatings under air suspended corundum particles

C.S. Ramachandran[a,*], V. Balasubramanian[a], P.V. Ananthapadmanabhan[b]

[a]*Department of Manufacturing Engineering, Annamalai University, Annamalai Nagar, Tamizhnadu 608 002, India*

[b]*Plasma Spray Technologies Section (PSTS), Laser and Plasma Technology Division (L&PTD), Bhabha Atomic Research Centre (BARC), Trombay, Mumbai 400 085, Maharashtra, India*

Received 6 April 2012; received in revised form 2 May 2012; accepted 26 June 2012
Available online 1 July 2012

Abstract

Atmospheric plasma sprayed (APS) zirconium oxide based coatings are used widely in aero engine components for providing thermal insulation, improving the corrosion and oxidation resistance. Despite its wide spread industrial use, little is known about the basic erosion behaviour and the mechanisms by which such coatings erode. In this paper, the erosive wear behaviours of Yttria Stabilized Zirconia (YSZ) coatings; Lanthanum Zirconate (LZ) coatings and Inconel 738 base material (BM) were studied and compared under air jet erosion conditions with corundum particles as erodent material. The erosion behaviour was studied with respect to the different porosity volume percentages of the coatings and the changes in velocity of erodent, impact angle of erodent and erodent particle flux. It was found that in solid particle erosion, the wear resistances of YSZ and LZ coatings were the best at their lowest porosity volume and it decreased with the increase in the percentage volume of porosity. There was a linear increase in the wear resistance with the increase in hardness. Further, relationships among the erosion parameters with respect to erosive wear loss were derived by using the response surface methodology and the erosion mechanisms were discussed adequately.

Keywords: B: Porosity; C: Hardness; C: Wear resistance; E: Engine components

1. Introduction

Thermal barrier coatings (TBCs) act to protect the coated components from the hot gases in a gas turbine engine. Degradation of the coating through the stepwise removal of material due to solid particle impact, either by ingested particles or particles generated by the engine itself, can result in localized hot spots and subsequent damage to, or reduced service life of, the component [1]. TBCs are more susceptible to erosion than fully dense ceramics, because their microstructure contains many crack-like features. Thus, erosion rates are expected to be higher for TBC than for their bulk ceramic counterparts. The literature pertaining to the solid particle erosion of APS TBCs is scant. As far as the recent literature survey is concerned only few authors have reported the erosion behaviour of APS YSZ TBCs.

Nicholls et al. compared the erosion behaviour of thermally sprayed and electron beam physical vapour deposited EB-PVD TBCs. The erosion studies have been carried out using nominally 100 μm alumina (particle size 80–120 μm) in tests at room temperature (20 °C) and 910 °C. The particle velocities for this grit were calculated to be 140 m/s at 20 °C and 230 m/s at 910 °C. Using this facility it was found, both at room temperature and 910 °C, that EB-PVD ZrO_2–8 wt% Y_2O_3 thermal barriers are significantly more erosion-resistant than the equivalent APS coatings, when impacted with either alumina or silica in the particle size range 40–100 μm. Examination of tested hardware reveals that cracking occurs within the near surface region of the columns for EB-PVD ceramic and that erosion occurs by the removal of these small blocks of material. In stark contrast, removal of material for plasma sprayed ceramic occurs through poorly bonded splat boundaries. At both room temperature and 910 °C, erosion

*Corresponding author. Tel.: +91 4144 230382; Mob.: +9843892693; fax: +91 4144 239734/238275.
E-mail addresses: csrcn@rediffmail.com, rcncs@yahoo.com (C.S. Ramachandran).

0272-8842/$36.00
http://dx.doi.org/10.1016/j.ceramint.2012.06.077

rates are linear with velocity for both types of coating. Peak erosion rates occur for normal impact, with impact angle dependence scaling similarly for the air plasma sprayed APS and EB-PVD coatings. At high temperatures, erosion rates are increased over those measured at room temperature [2].

Janos et al. investigated the erosion behaviour of air–plasma-sprayed 7YSZ TBC at elevated temperatures. The paper focused on both the porosity of the coating as well as the thermal pre-treatment of the ceramic. To simulate operating conditions on the ceramic samples, high temperature erosion experiments at 1093 °C were carried out on as-sprayed samples as well as on samples, thermally aged at different temperatures up to 1482 °C in air prior to erosion testing. Alumina grit with a mean size 27 μm was used as erodent material. The incident angle was 30° and the erosion velocity was 244 m/s. A significant dependence of erosion rate on porosity and thermal pre-treatment was found. The heat treated sample had a lower erosion rate compared to the as sprayed ones. Erosion rates seem to be highly correlated to the micro-hardness of the zirconia TBC [3].

Pi-Chuen et al. studied the effect of pulsed CO_2 laser glazing on APS YSZ TBCs. The subsequent effects of laser glazing on the microstructure and erosion behaviour of applied coatings were then evaluated by the authors. Several erosion tests were conducted at room temperature using 50 μm silica erodent particles with impact velocity of 50 m/s. The results of their investigation showed that the laser-glazing process increased the micro-hardness from about 550 HV for the as-sprayed layer to about 1550 HV for the as-glazed layer. The erosion rate increased as the impingement angle increased for both plasma-sprayed and laser-glazed TBCs. Laser glazing enhanced the erosion resistance of plasma-sprayed TBCs by about 1.5 to 3 times with the impingement angle ranging between 30° and 75°, while the erosion resistance did not significantly improve when the impingement angle reached 90°. Erosion morphology analysis clearly indicated that the erosion of the plasma-sprayed TBCs was deemed to be the erosion of the protrusions and the sprayed splats. The erosion of the laser-glazed TBCs was proven to be the spallation of the glazed layer. Spallation occurred in the laser-glazed layer/plasma-sprayed splats interface [4].

Cernushi et al. compared the erosion rates of one standard porous APS, two segmented APS, one EB-PVD and one plasma spray physical vapour deposition (PS-PVD) YSZ coatings tested in a solid particle erosion jet tester, with EB-PVD and standard porous APS YSZ coatings being the two reference systems. The testing temperature, impingement angles and impingement velocity have been set up equal to 700 °C, 30° and 90° and 40 ± 5 m/s, respectively. Microquartz (SiO_2 in the crystallographic hexagonal phase) powder ($d_{10}=68$ μm, $d_{50}=122$ μm, $d_{90}=204$ μm) was used as erosive particles, quartz being one of the main erosive constituents of sand and fly volcanic ashes. Furthermore, the feed rate of erosive particles was set up to 2 g/min. After the end of the tests, the TBC microstructure was investigated using electron microscopy to characterise the failure mechanisms taking place in the TBC. It was found that PS-PVD and highly segmented TBCs showed erosion rates comparable or better than EB-PVD samples [5].

TBCs using 7–8 wt% yttria partially stabilised zirconia (YSZ) as the top coat have been used in gas turbine engines traditionally and it is widely accepted that it offers high strain compliance. Unfortunately, the YSZ coating undergoes phase transformation and sintering when exposed above 1200 °C, which also leads to a coating with a higher thermal conductivity. Hence the challenge is to lower the thermal conductivity of TBCs to provide a coating with excellent thermal properties above 1200 °C [6]. There are several ceramic materials that have been evaluated as high temperature TBC materials, and lanthanum zirconate (LZ) is one of the most promising among them.

The properties of high melting point, phase stability up to its melting point, low thermal conductivity, low sintering ability and oxygen-non transparent are the major reasons for the belief that lanthanum zirconate has potential as TBC material for high-temperature applications [7]. It is essential that the significance of particulate erosion as a life-limiting factor be assessed for new generation TBC materials. For any erosive wear situation, process parameters such as the particle impact velocity, the angle of particle impact relative to the surface and the particle feed rate (particle flux) are expected to have a significant effect on the wear rate of the material under investigation. Furthermore, for plasma sprayed ceramic coatings, the presence of porosity in the coatings may also have important influences on erosion. However, the authors are not aware of any work published on the erosion of LZ TBCs.

From the literature survey it was understood that, no systematic, quantitative studies have been performed on the comparative evaluation of the effect of process parameters on the erosion behaviour of YSZ coatings, LZ coatings and the base metal Inconel 738. In order to detect and quantify the strength of the effect of each of the variables, the methods of statistical experimental design may be used. A central composite design provides a thorough method for determining all the interactions within the range of conditions of interest [8]. This approach can also be used to generate an empirical expression for the response (here the resistance to erosive wear) in terms of the variables studied. This paper reports the use of a central composite experimental design to study and compare the erosion durability of a typical YSZ coating with LZ coatings and the base metal Inconel 738 in terms of the erodent particle impact velocity, the angle of erodent particle impact relative to the surface, the erodent particle flux and the vol% of porosity in the coatings during the test.

2. Experimental details

2.1. Preparation and characterization of coatings

An agglomerated and sintered Yttria Stabilized Zirconia (YSZ) spherical powder (Fig. 1) with size ranging between 10–45 μm (H.C. Stark, AMPERIT 827.054 powder (ZrO_2,

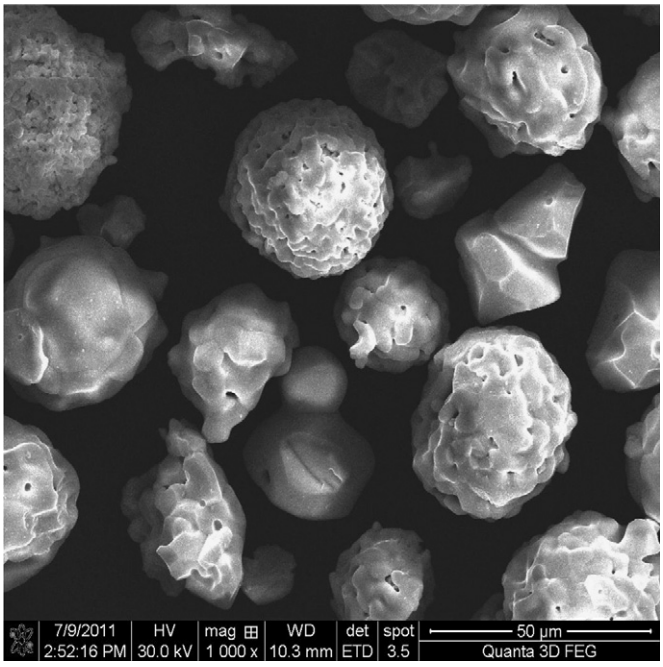

Fig. 1. Agglomerated and sintered YSZ powder.

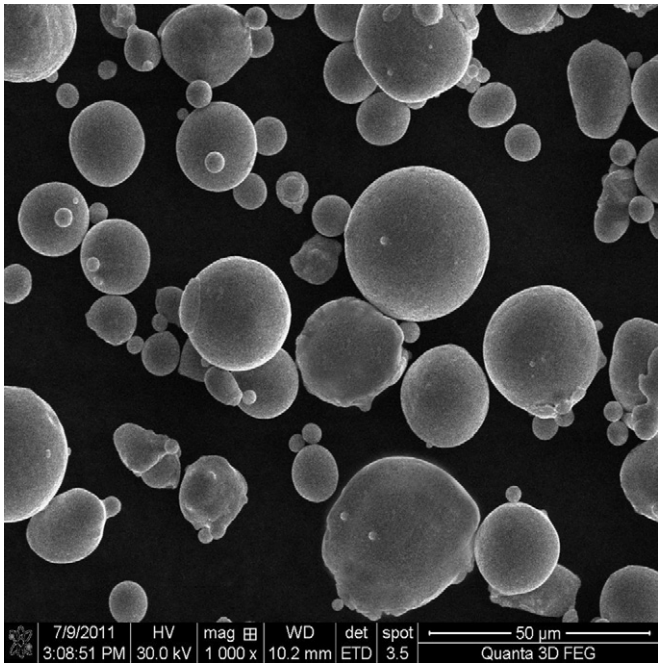

Fig. 2. Synthesised and spheroidized LZ powder.

7 wt% Y_2O_3)) was used. Since, the Lanthanum Zirconate (LZ) powder is not commercially available; the LZ powder (Fig. 2) was prepared in our laboratory. The plasma spray deposition of the YSZ and the synthesised LZ powders were carried out using a semi-automatic 40 kW IGBT-based Plasmatron (Make: Ion Arc Technologies; India. Model: APSS-II). The porosity of the coatings were analysed as per ASTM B276 standard on the polished cross-section of the coating, using optical microscope (Make: Meiji; Japan, Model: MIL-7100) equipped with image analysing system.

Customary metallographic procedures were adopted to polish the cross-section of the coatings. A 200 µm square area was selected on the polished cross-section of the coating, and the image was analysed. The same procedure was repeated at five random locations to find out the average percentage volume of porosity. Coatings were subjected to SEM and EDS mapping analysis (Make: Quanta; Switzerland. Model: 3D FEG). The top and cross-sectional morphologies of LZ and YSZ coatings deposited with different porosity levels are shown in Figs. 3 and 4, respectively. Fig. 5 displays the EDS mapping analysis carried out at the cross-sections of LZ and YSZ coatings, which shows the uniform distribution of elements in the coatings. The XRD analysis (Make: Rigaku; Japan. Model: ULTIMA-III) of the as deposited coatings are shown in Fig. 6. The AFM analyses of the eroded specimens were conceded by means of (Make: JPK, London. Model: Nano Wizard II) Si probes operated under non tapping mode. The LZ coating has cubic pyrochlore phase (Fig. 6a) and the YSZ coating has tetragonal prime (t′) phase (Fig. 6b). The microhardness measurement was made using a Vickers micro-hardness tester (Make: Shimadzu; Japan. Model: HMV-2T). A load of 300 g and a dwell time of 15 s were used to evaluate the hardness. Hardness values were measured at 10 random locations on the polished cross-section of a coating. The tensile bond strength test was carried out as per ASTM C 633 standard and the lap shear bond strength was carried out using EN1465 standard using a universal testing machine (Make: FIE Blue Star; India. Model: UNITEK-94100). A commercially available heat curable epoxy was used as an adhesive, to test the coated specimens. For erosion test specimens, the ceramic powders were directly sprayed on to the faces of $12.25 \times 25.4 \times 3$ mm (L × B × H) grit-blasted Inconel 738 coupons but bond coat was not used. The hardness of the un-coated IN 738 coupon was 381 $HV_{0.3}$. Different combinations of APS process parameters were used to incorporate different volume percentages of porosity in the coatings. Coating thickness for all the deposits was maintained at 350 ± 15 µm. The APS process parameter settings to attain different levels of porosity in the coatings with their corresponding mechanical property values are shown in Table 1. The method of preparing the plasma spray quality LZ power, the detailed characterization and optimization of APS process parameters to attain different volume percentages of porosity in the coatings are available elsewhere [9,10].

2.2. Erosion testing of specimens

The solid particle erosion tests were carried out in an air jet erosion testing machine (Make: DUCOM; India. Model: TR 470) shown in Fig. 7 as per ASTM G76-07 standard. Corundum particles (50 µm particle size)

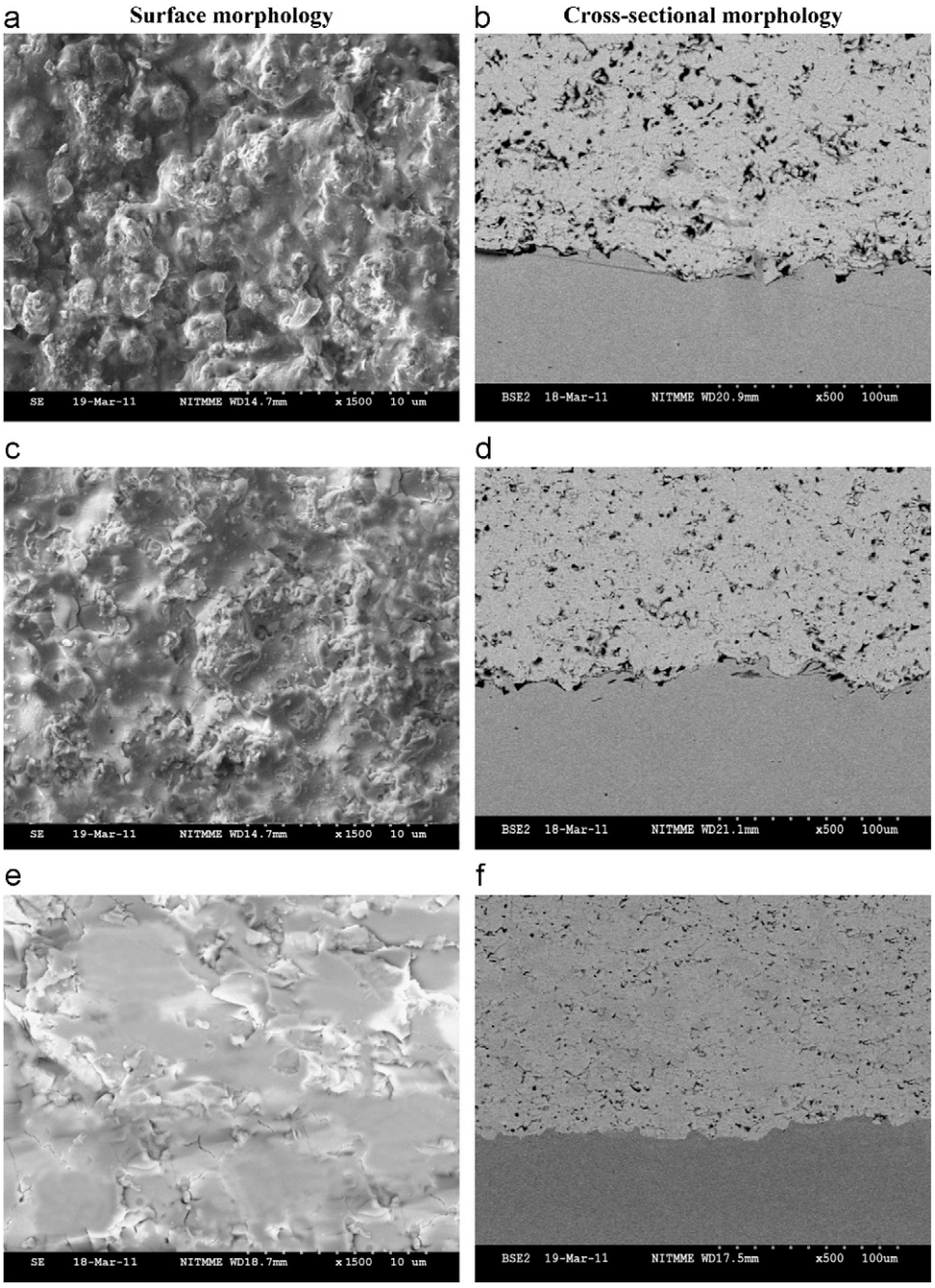

Fig. 3. Surface and cross-sectional morphology of LZ coatings produced with 24 vol% porosity: (a) and (b); 14 vol% porosity: (c) and (d) and 4 vol% porosity: (e) and (f).

were used as the erodent (Fig. 8a) and were fed by a particle feeder at a controlled rate into the mixing chamber where they entrained the dry high velocity air coming from the compressor. The particles moved with the air stream through a tungsten carbide nozzle. The inner diameter of the nozzle is 1 mm while the nozzle length is 35 mm. The working distance between the nozzle and the specimen surface is 10 mm. The particles accelerate through the nozzle and then finally hit the sample kept fixed on the sample holder. The velocities of the impinging particles were measured using the well-known double-disc method. The impact angles were varied by simply varying the orientation of the sample surface with respect to the impinging particles stream. The erosion test samples, both coated and uncoated samples were lapped using 1 μm diamond lapping paste which ensured consistency in surface finish to an Ra of 0.05 μm. After lapping, each sample was ultrasonically cleaned in acetone. The cleaned samples were dried and then weighed using an electronic balance (Make: Shimadzu; Japan. Model: AW 320) having a resolution of 0.01 mg.

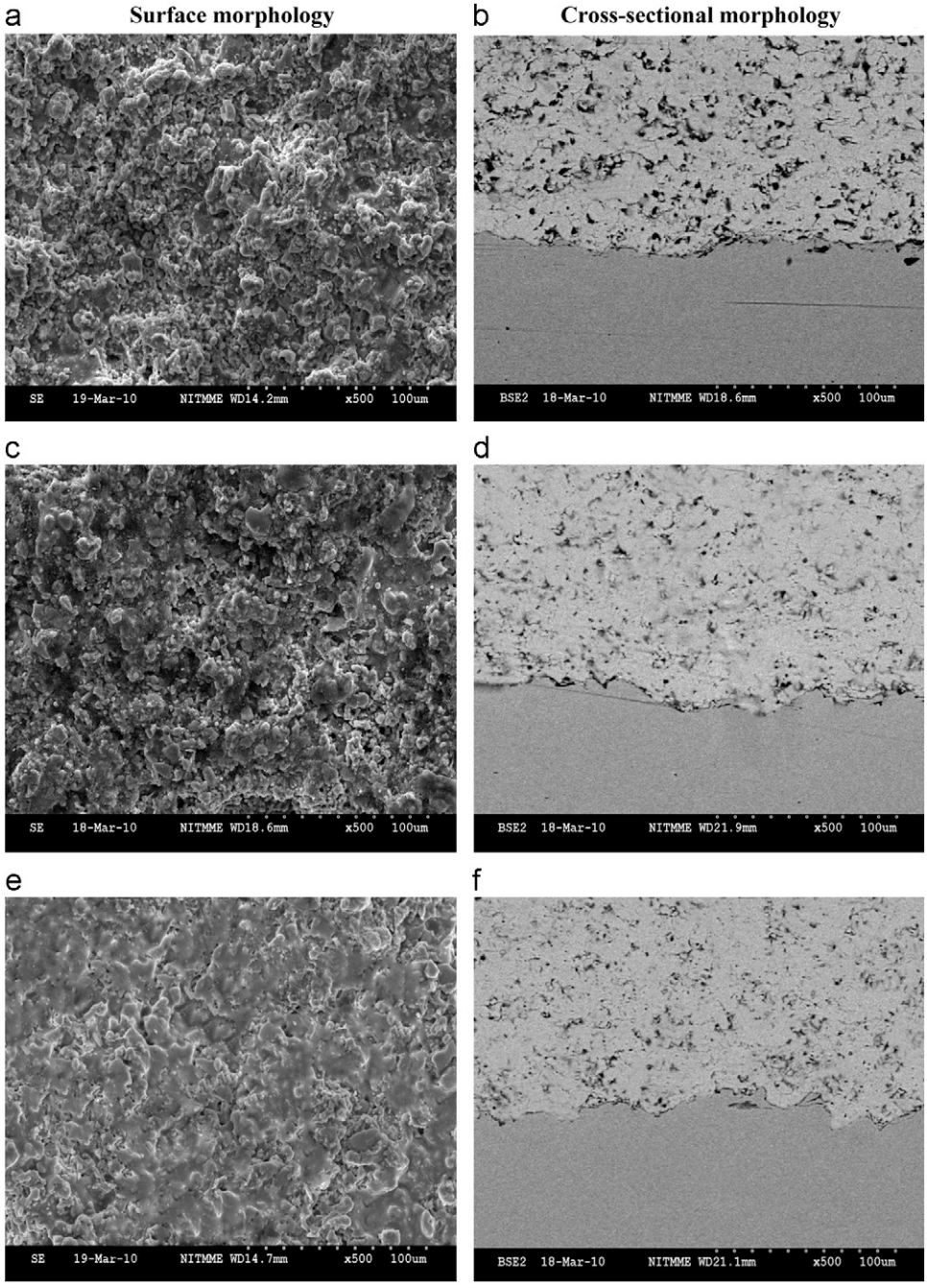

Fig. 4. Surface and cross-sectional morphology of YSZ coatings produced with 24 vol% porosity: (a) and (b); 14 vol% porosity: (c) and (d) and 4 vol% porosity: (e) and (f).

The sample was next fixed to the sample holder of the erosion rig and eroded with corundum particles at the predetermined particle feed rate, impact velocity and impact angle for a period of about 2 min. The sample was then removed, cleaned in acetone and dried and weighed to determine the weight loss. This weight loss normalised by the mass of the corundum particles causing the weight loss was then defined as the incremental erosion rate. The above procedure was repeated till the incremental erosion rate attained a constant value independent of the mass of the erodent particles or, equivalently, of testing time. This constant value of the incremental erosion rate was defined as the steady-state erosion rate. After considering all of the aforementioned conditions, the feasible limits of the parameters were chosen so that wear test could be conducted without any difficulty. A central composite rotatable design of second order was found to be the most efficient tool in response surface methodology (RSM) to establish the empirical relationship of the response surfaces using the smallest possible number of experiments without a loss of accuracy [11]. Due to a wide range of factors, the use of a three factors and five-level

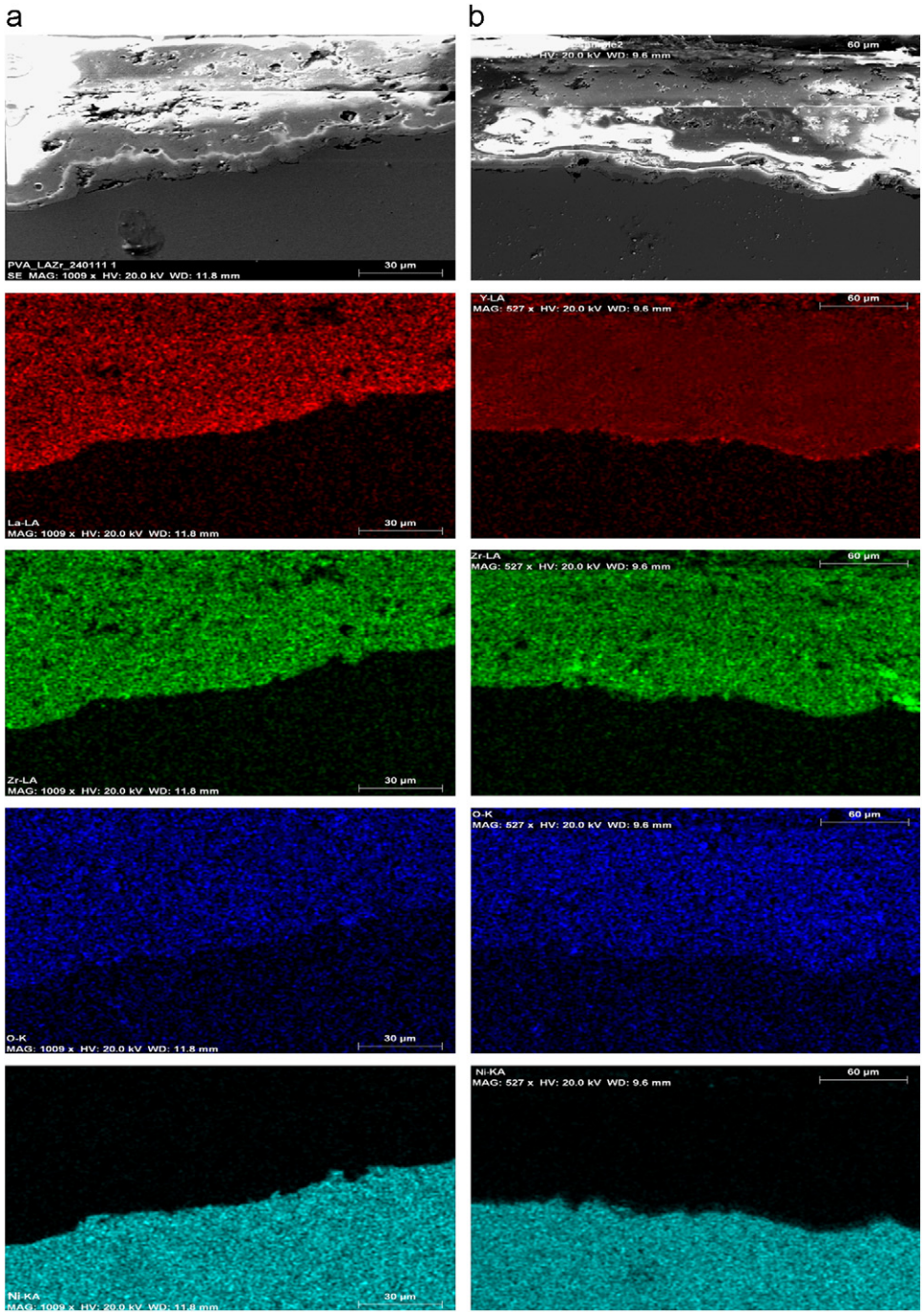

Fig. 5. EDS elemental mapping analysis of the cross-section of the as deposited coatings. (a) Figure 5a LZ coating; (b) Figure 5b YSZ coating.

central composite design matrix was chosen to conduct the wear tests for the substrate material and a four-factors five level central composite design matrix was chosen to conduct the erosion tests for the coatings. With a view to study the effects of the considered process parameters on the erosion rate, statistically designed experiments, based on a factorial technique, were used to reduce the cost and time and to obtain the required information pertaining to the main and the interaction effects of the parameters on the response. The factors and their ranges considered for the erosion test pertaining to the substrate and the coatings are shown in the Tables 2 and 3, respectively. Tables 4 and 5 show the coded conditions of the erosion test factors and their levels, which were used to form the design matrices for the substrate and the coatings, respectively. The first 8 conditions in Table 4 and the first 16 conditions in Table 5 are corner points derived from the half factorial design. All of the variables at the intermediate (0) level constitute the centre points while the combinations of each process variable at either the lowest (−1.68 in Table 4 and −2

in Table 5) or highest (+1.68 in Table 4 and +2 in Table 5) value with the other variables of the intermediate levels constitute the star points. For the convenience of recording and processing experimental data, the upper and lower levels of the factors are coded here as −1.68, +1.68 in Table 4 and −2, +2 in Table 5, respectively. The coded values of any intermediate value can be calculated using the following relationship:

$$\mathbf{X_i} = \{\mathbf{2}[2\mathbf{X} - (\mathbf{X_{max}} + \mathbf{X_{min}})]/(\mathbf{X_{max}} - \mathbf{X_{min}})\} \quad (1)$$

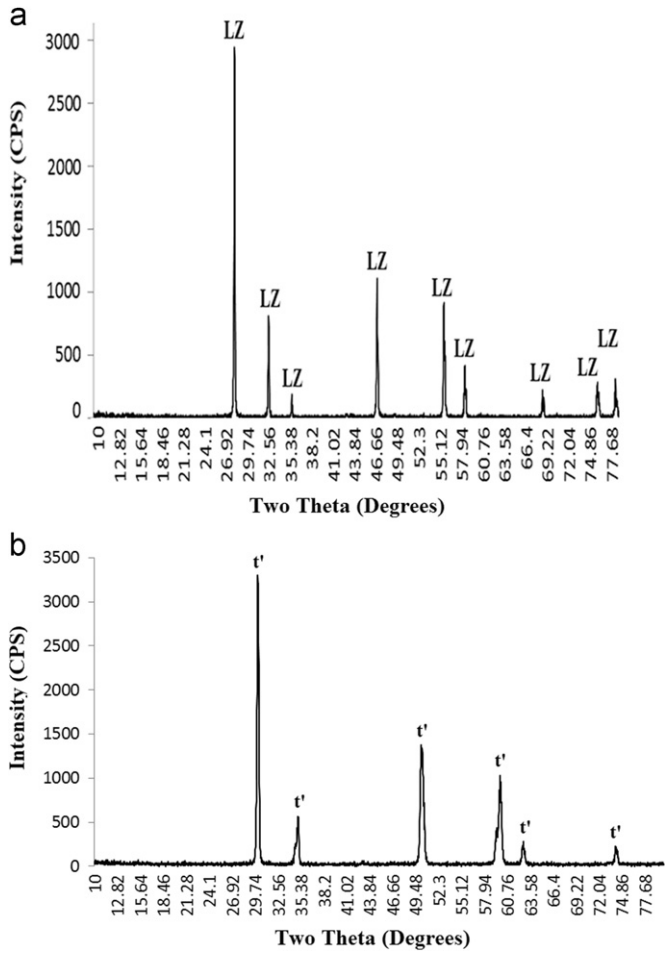

Fig. 6. XRD patterns of the as deposited coatings.

here, X_i is the required coded value of a variable X; X is any value of the variable from X_{min} to X_{max}; X_{min} is the lower level of the variable; X_{max} is the highest level of the variable.

In this investigation, the erosion tests were conducted as prescribed by the experimental design matrices (Tables 4 and 5). The experiments were conducted in a random order to prevent systematic errors from infiltrating the response of the system. At least three tests were carried out at each experimental condition to ensure reliability of the results. The images of the specimens after erosion tests are shown in Fig. 8b–d.

3. Predictive statistical model for erosion rate

In this study, a response surface model-building technique was utilized to predict the erosion rate in terms of the vol% of porosity present in the coatings, the velocity of the erodent particle, the angle of impact of the erodent particle and the erodent particle flux. Details of the model building technique are discussed below.

3.1. Response surface methodology (RSM)

RSM is an experimental strategy that explores the space of the process independent variables, and an empirical statistical modelling, to develop an appropriate relationship between the responses (output) and the process variables or factors (input). In the present investigation, to correlate the process parameters and the wear rates, an empirical relationship was developed to predict the responses based on experimentally measured values. The responses are a function of vol% of porosity present in the coatings (P), velocity of the erodent particle (V), angle of impact of the erodent particle (A) and erodent particle flux (F) and it can be expressed as

$$\mathbf{Responses} = \{\mathbf{f}(\mathbf{P}, \mathbf{V}, \mathbf{A}, \mathbf{F})\} \quad (2)$$

The empirical relationship chosen includes the effects of the main and interaction effect of all factors. The construction of empirical relationship and the procedure to calculate the values of the regression coefficients can be

Table 1
Optimised APS process parameters settings to attain different volume percentages of porosity in the coatings with the respective mechanical properties.

Factor/ Response	Optimised levels and response values of YSZ/LZ				
Power (kW)	26/25	26/24	24/22	24/21	22/21
Primary gas flow rate (lpm)	36/35	36/32	31/32	26/25	29/29
Stand of distance (mm)	111/111	114/112	100/116	114/117	119/103
Powder feed rate (gpm)	23/20	20/19	21/21	27/25	29/33
Carrier gas flow rate (lpm)	8/9	8/9	8/8	7/8	7/7
Porosity (vol%)	4	8	14	20	24
Microhardness ($HV_{0.3}$)	1149/1184	1052/1097	867/954	712/831	659/708
Tensile bond strength (MPa)	21/19	17/16	15/12	9/8	7/5
Lap shear bond strength (MPa)	11/10	8/7	7/6	5/4	4/3

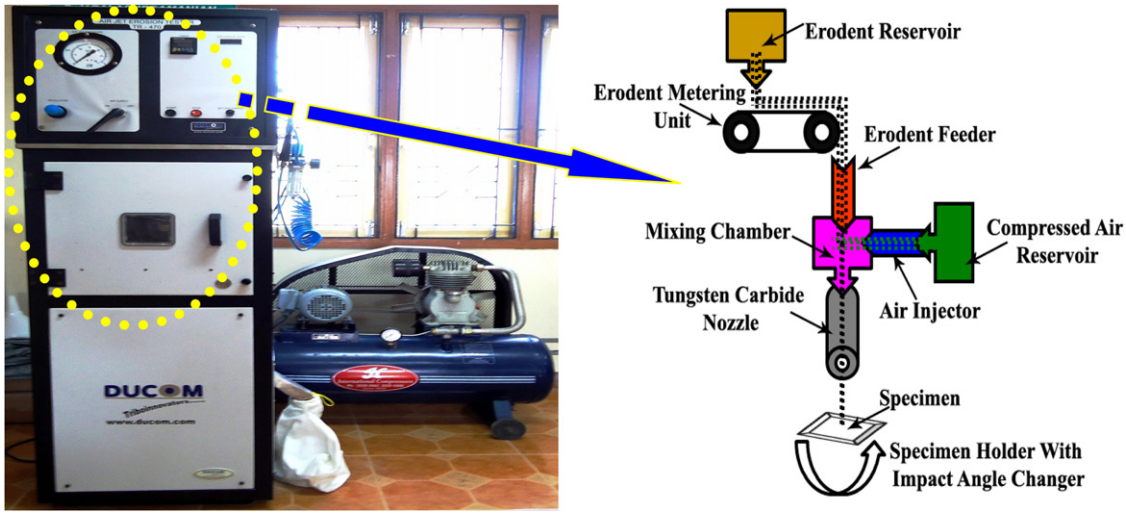

Fig. 7. Air jet erosion test rig with the respective schema.

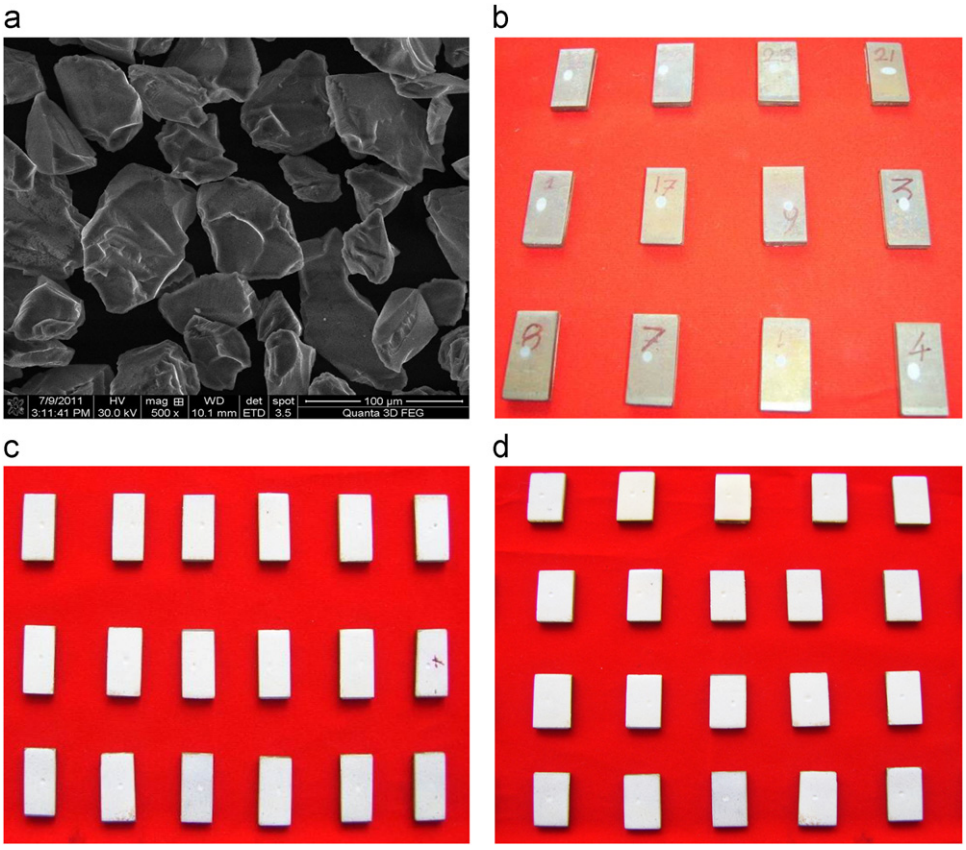

Fig. 8. Images of the erodent and the eroded specimens. (a) Corundum abrasive erodent powder used for erosion test; (b) Inconel 738 substrate after erosion; (c) YSZ coated specimens after erosion; (d) LZ coated specimens after erosion.

referred elsewhere [12]. In this work, the regression coefficients were calculated with the help of Design Expert V 8.1 statistical software. After determining the coefficients (at a 95% confidence level), the final empirical relationships were developed using these coefficients. The final empirical relationships to estimate the responses are given below:

$$\textbf{Erosion Rate of Bare Inconel } 738 \textbf{ Substrate (gpg)} = \{\mathbf{0}.060172 + \mathbf{0}.020892\ (\mathbf{V}) - \mathbf{0}.0198\ (\mathbf{A}) - \mathbf{0}.01566\ (\mathbf{F})\} \quad (3)$$

Table 2
Considered factors for solid particle erosion test and their levels for uncoated Inconel 738 substrate.

Factors	Notations	Units	Level				
			Lowest (−1.68)	Low (−1)	Middle (0)	High (+1)	Highest (+1.68)
Velocity of the erodent particle	V	(m/s)	20	36.19	60	83.81	100
Angle of impact of the erodent particle	A	(°)	30	42.20	60	77.85	90
Erodent particle flux	F	(gpm)	2	2.81	4	5.19	6

Table 3
Considered factors for solid particle erosion test and their levels for YSZ and LZ coatings.

Factors	Notations	Units	Level				
			Lowest (−2)	Low (−1)	Middle (0)	High (+1)	Highest (+2)
Porosity of the coating	P	(vol%)	4	9	14	19	24
Velocity of the erodent particle	V	(m/s)	20	40	60	80	100
Angle of impact of the erodent particle	A	(°)	30	45	60	75	90
Erodent particle flux	F	(gpm)	2	3	4	5	6

Table 4
Experimental design matrix for solid particle erosion test of uncoated Inconel 738 substrate with results (Factors are in coded values).

Erosion test condition	Velocity of the erodent particle	Angle of impact of the erodent particle	Erodent particle flux	Erosion rate of uncoated Inconel 738 substrate (gpg)
1	−1	−1	−1	0.0604
2	1	−1	−1	0.1361
3	−1	1	−1	0.0298
4	1	1	−1	0.0717
5	−1	−1	1	0.0384
6	1	−1	1	0.0781
7	−1	1	1	0.0161
8	1	1	1	0.0375
9	−1.68	0	0	0.0264
10	1.68	0	0	0.0898
11	0	−1.68	0	0.0891
12	0	1.68	0	0.0222
13	0	0	−1.68	0.0852
14	0	0	1.68	0.0341
15	0	0	0	0.0601
16	0	0	0	0.0568
17	0	0	0	0.0655
18	0	0	0	0.0564
19	0	0	0	0.0657
20	0	0	0	0.0567

$$\textbf{Erosion Rate of YSZ Coating (gpg)} = \{\mathbf{0}.143223 + \mathbf{0}.048488\ (\mathbf{P}) + \mathbf{0}.024563\ (\mathbf{V}) + \mathbf{0}.021146\ (\mathbf{A}) - \mathbf{0}.01191\ (\mathbf{F})\} \quad (4)$$

$$\textbf{Erosion Rate of LZ Coating (gpg)} = \{\mathbf{0}.10735 + \mathbf{0}.031921\ (\mathbf{P}) + \mathbf{0}.016171\ (\mathbf{V}) + \mathbf{0}.013921\ (\mathbf{A}) - \mathbf{0}.00784\ (\mathbf{F})\} \quad (5)$$

4. Results

4.1. Checking the adequacy of the empirical relationships

In this investigation, analysis of variance (ANOVA) is used to check the adequacy of the developed empirical relationships. ANOVA test results of the erosion rate of uncoated substrate, YSZ coating and LZ coating are presented in Tables 6, 7 and 8, respectively. From the *F* value assessment

Table 5
Experimental design matrix for solid particle erosion test of coatings with results (Factors are in coded values).

Erosion test condition	Porosity of the coatings	Velocity of the erodent particle	Angle of impact of the erodent particle	Erodent particle flux	Erosion rate of YSZ coating (gpg)	Erosion rate of LZ coating (gpg)
1	−1	−1	−1	−1	0.0614	0.0535
2	1	−1	−1	−1	0.1528	0.1136
3	−1	1	−1	−1	0.1196	0.0918
4	1	1	−1	−1	0.2059	0.1486
5	−1	−1	1	−1	0.1014	0.0798
6	1	−1	1	−1	0.2056	0.1484
7	−1	1	1	−1	0.1567	0.1162
8	1	1	1	−1	0.2522	0.1791
9	−1	−1	−1	1	0.0389	0.0387
10	1	−1	−1	1	0.1398	0.1051
11	−1	1	−1	1	0.0853	0.0692
12	1	1	−1	1	0.1889	0.1374
13	−1	−1	1	1	0.0858	0.0696
14	1	−1	1	1	0.1757	0.1287
15	−1	1	1	1	0.1278	0.0972
16	1	1	1	1	0.2211	0.1586
17	−2	0	0	0	0.0452	0.0428
18	2	0	0	0	0.2445	0.1741
19	0	−2	0	0	0.0947	0.0754
20	0	2	0	0	0.1914	0.1391
21	0	0	−2	0	0.1012	0.0797
22	0	0	2	0	0.1881	0.1369
23	0	0	0	−2	0.1612	0.1192
24	0	0	0	2	0.1144	0.0884
25	0	0	0	0	0.1445	0.1082
26	0	0	0	0	0.1348	0.1018
27	0	0	0	0	0.1447	0.1083
28	0	0	0	0	0.1341	0.1013
29	0	0	0	0	0.1447	0.1083
30	0	0	0	0	0.1343	0.1015

Table 6
ANOVA test results for erosion rate of uncoated Inconel 738 substrate.

Source	Sum of squares	*Df*	Mean square	*F* value	*p*-value prob > *F*	
Model	0.015563	9	0.001729	100.8402	< 0.0001	significant
Velocity of the erodent particle	0.005961	1	0.005961	347.6223	< 0.0001	
Angle of impact of the erodent particle	0.005354	1	0.005354	312.2322	< 0.0001	
Erodent particle flux	0.003348	1	0.003348	195.2551	< 0.0001	
Residual	0.000171	10	1.71E-05			
Lack of fit	7.49E-05	5	1.5E-05	0.775195	0.6066	Not significant
Pure error	9.66E-05	5	1.93E-05			
Cor. total	0.015735	19				
Std. dev.	0.004141					
Mean	0.058805					
C.V.%	7.042022					
R-squared	0.989102					
Adj R-squared	0.979293					
Pred R-squared	0.952017					

Df: degrees of freedom; CV: co-efficient of variation; *F*: Fisher ratio; *p*: probability.

shown in Tables 6–8, it was found that the predominant factors which have direct influence on the responses as per hierarchy are vol%. of porosity present in the coating, velocity of the erodent particle, angle of impact of the erodent particle and erodent particle flux, respectively. The determination coefficient (R^2) indicates the goodness of fit for the model. In all the cases, the value of the determination coefficient ($R^2 > 0.99$) indicates that less than 1% of the total variations is not explained by the empirical relationships. The value of the adjusted determination coefficient is also high, which indicates the high significance of the empirical relationships. The predicted R^2 values also show good agreement with the

Table 7
ANOVA test results for erosion rate of YSZ coating.

Source	Sum of squares	*Df*	Mean square	*F* value	*p*-value prob > *F*	
Model	0.085042	4	0.02126	836.9965	< 0.0001	significant
Porosity of the coatings	0.056425	1	0.056425	2221.376	< 0.0001	
Velocity of the erodent particle	0.01448	1	0.01448	570.043	< 0.0001	
Angle of impact of the erodent particle	0.010732	1	0.010732	422.4858	< 0.0001	
Erodent particle flux	0.003406	1	0.003406	134.0813	< 0.0001	
Residual	0.000635	25	2.54E-05			
Lack of fit	0.000478	20	2.39E-05	0.758815	0.7035	not significant
Pure error	0.000157	5	3.15E-05			
Cor. total	0.085677	29				
Std. dev.	0.00504					
Mean	0.143223					
C.V.%	3.51893					
R-squared	0.992588					
Adj R-squared	0.991402					
Pred R-squared	0.989797					

Df: degrees of freedom; CV: co-efficient of variation; *F*: Fisher ratio; *p*: probability.

Table 8
ANOVA test results for erosion rate of LZ coating.

Source	Sum of squares	*Df*	Mean square	*F* value	*p*-value prob > *F*	
Model	0.036856	4	0.009214	833.3251	< 0.0001	significant
Porosity of the coatings	0.024455	1	0.024455	2211.72	< 0.0001	
Velocity of the erodent particle	0.006276	1	0.006276	567.6055	< 0.0001	
Angle of impact of the erodent particle	0.004651	1	0.004651	420.6416	< 0.0001	
Erodent particle flux	0.001474	1	0.001474	133.3328	< 0.0001	
Residual	0.000276	25	1.11E-05			
Lack of fit	0.000208	20	1.04E-05	0.764162	0.6999	not significant
Pure error	6.81E-05	5	1.36E-05			
Cor. total	0.037132	29				
Std. dev.	0.003325					
Mean	0.10735					
C.V.%	3.09751					
R-squared	0.992556					
Adj R-squared	0.991365					
Pred R-squared	0.989749					

Df: degrees of freedom; CV: co-efficient of variation; *F*: Fisher ratio; *p*: probability.

adjusted R^2 values. The value of probability $> F$ in Tables 6, 7 and 8 for the empirical relationship is less than 0.05, which indicates that the empirical relationships are significant. Lack of fit is not significant for all the developed empirical relationships as it is desired [13]. The normal probability plots for the responses were analysed and the errors were found to be distributed normally. Collectively, these results indicate the excellent capability of the regression model. The developed empirical relationships can be effectively used to predict the responses by substituting the process parameter values in coded form.

4.2. Analysis of perturbation plots

The developed empirical relationships were used to study the effects of porosity, velocity, angle of impact and flux on the erosion rate. Based on these empirical relationships, the main and interaction effects of the process parameters on the wear rates were computed and plotted in the form of perturbation plots, as shown in Fig. 9. The perturbation plot is an important diagrammatic representation which provides silhouette views of the response surface. The perturbation plot can be used to compare the effects of all factors at a particular point in the RSM design space. For response surface designs, the perturbation plot shows how the response changes as each factor moves from the chosen reference point, while all other factors remain constant at the reference value.

Normally, Design-Expert software sets the reference point default at the middle of the design space (the coded zero level of each factor). A steep slope or curve in a factor shows that the response is sensitive in that factor. A relatively flat line shows insensitivity to change in that particular factor [14]. It is clear from Fig. 9 that the

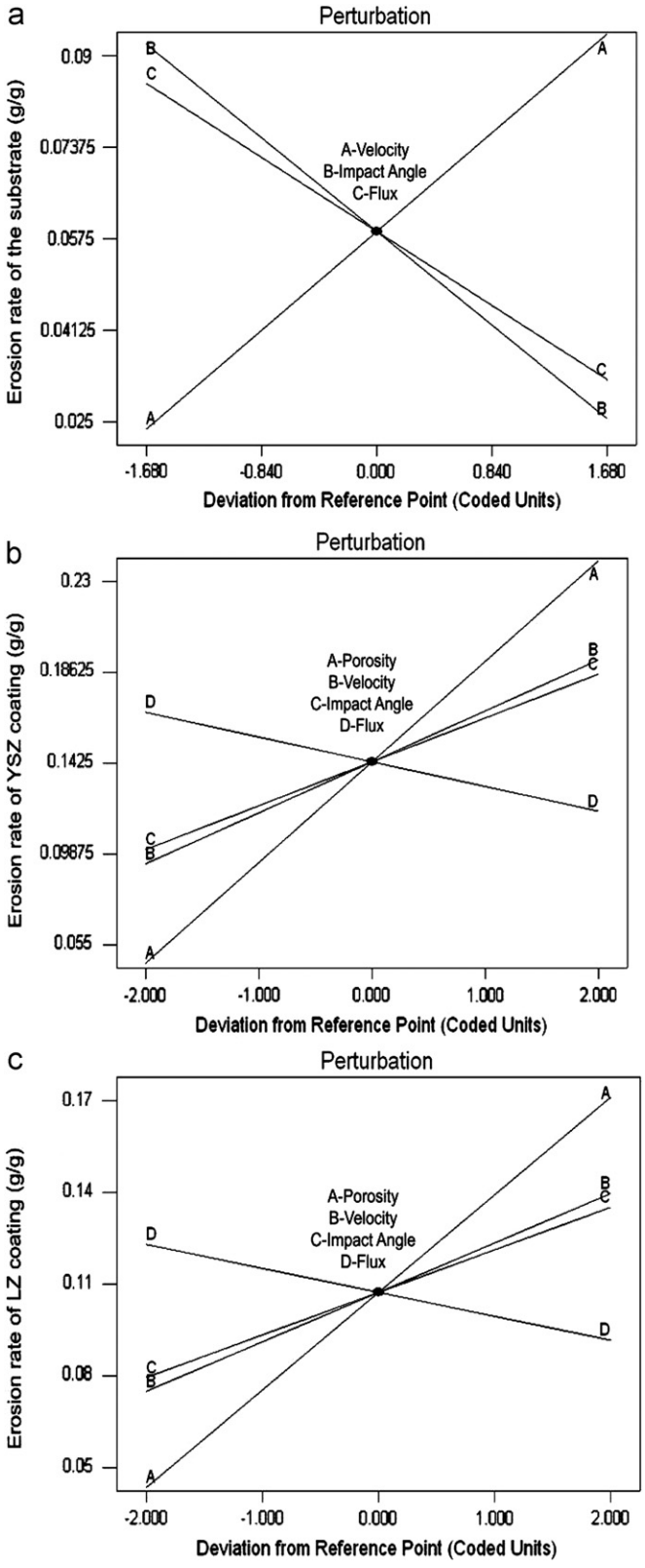

Fig. 9. Perturbation plots for the erosion rate of specimens with respect to solid particle erosion test parameters. (a) Inconel 738 substrate; (b) YSZ coating; (c) LZ coating.

erosion rate increases, with the increase of the levels of factors (porosity present in the coatings, velocity of the erodent particle, angle of Impact of the erodent particle and erodent particle lux) under consideration. The apex of the perturbation plot shows the maximum erosion rate. These plots can help in the prediction of the response for any zone of the experimental domain.

5. Discussions

5.1. Effect of erodent particle velocity on erosion rate

These perturbation plots (Fig. 9) show that the erosion rate increased with the increase in the impact velocity of the erodent particles. It is generally recognized that

$$\textbf{Erosion} = \{\mathbf{K} \times (\textbf{velocity})^{\mathbf{n}}\} \quad (6)$$

where constant '**K**' depends upon impact angle and particle size and '**n**' is the velocity exponent. In the gas-blast tester the particle velocity is not uniform across the diameter of the emerging particle jet [15]. As may be clearly seen, the maximum velocity occurs at the centre of the jet and falls off rapidly as the outer edges are approached. Given the power law relationship between the erosion rate and particle velocity, a small decrease in particle velocity will, therefore, result in an amplified reduction of the erosion rate.

5.1.1. Erosion under low erodent particle velocity conditions

When the velocity is decreased, the kinetic energy transferred to the particle is decreased. The lower the kinetic energy, the less the chance of a positive result (the erosion decreases) from a single impact. Further, under low velocities the particle jet divergence increases under such circumstances. These particles impinge upon the surface with low kinetic energies, or at unfavourable incidence angles, or have most of their translational kinetic energy turned into rotational kinetic energy (particle rotation) [16]. Hence the material removal will be minimum as could be inferred from Fig. 9. As the impact energy is lowered and less lateral cracks are generated in the lamellae of the ceramic coatings as seen in Fig. 10a and b. At the lowest energy, lateral cracks were rare and never smooth (like you see when a new lateral crack removes a chip). When particle speed is decreased, eventually the particles are not able to initiate cracking and will only plastically deform the coatings as displayed in Fig. 10a and b.

In the case of the uncoated substrate, the low forward momentum of the particle means that it will tend to roll on the target surface resulting in little surface deformation and small lips as seen in Fig. 10c. During the low impact velocity conditions, there are two possibilities for the cutting wear to cease [17]:

- The cutting ceases when the particle tip can no longer move forward, that is, when the tangential component of velocity becomes zero.
- The cutting may also cease when a release of elastic stresses in the surface of the target material takes place, because of which the particle rebounds off the target surface.

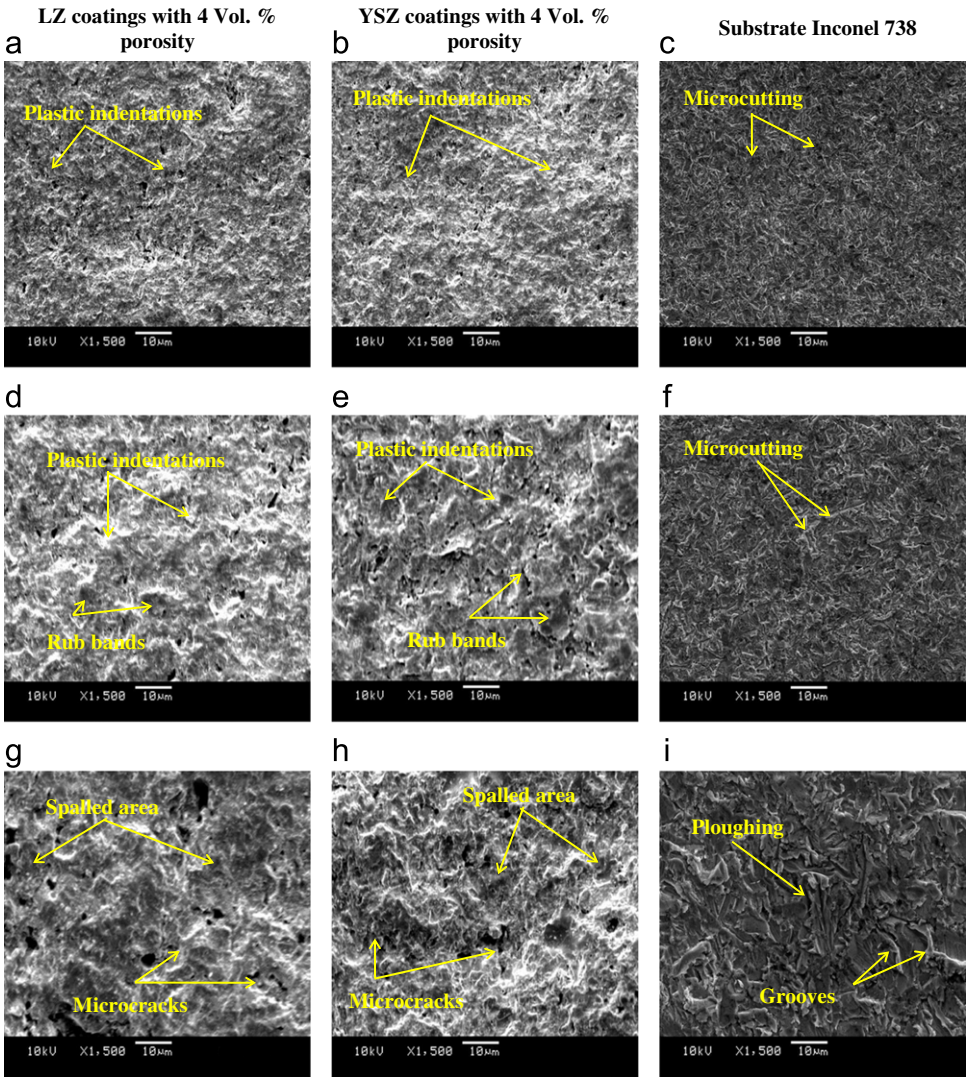

Fig. 10. Worn surfaces of coatings and substrate under different erodent particle velocities. (a-c) Velocity of the erodent particle: 20 m/sec; Impact angle of the erodent particle: 60°; Erodent particle flux: 4 gpm; (d-f) Velocity of the erodent particle: 60 m/sec; Impact angle of the erodent particle: 60°; Erodent particle flux: 4 gpm; (g-i) Velocity of the erodent particle: 100 m/sec; Impact angle of the erodent particle: 60°; Erodent particle flux: 4 gpm.

The two points mentioned above will decrease the wear rate of the coatings as well as the uncoated substrate under low velocity conditions. One can also witness in Fig. 10d and e that under a velocity of 60 m/s the plastic indentations and the rub bands are deeper compared to lower velocity condition. The worn surface of BM exposed under a velocity of 60 m/s shown in Fig. 10f possesses deep microcuts compared to the surface impacted with 20 m/s impact velocity.

5.1.2. Erosion under high erodent particle velocity conditions

With the higher initial velocity of particle shown in Fig. 9, the erosion rate appears to increase explicitly. This suggests the erosion rate to be nearly proportional to the square of velocity or the kinetic energy of particle. The relative variability appears to decrease at higher particle velocity. Though not conclusive, it may be due to the fact that larger areas are removed under the higher velocity impact. It might be expected that the shear force applied by the particle would increase as a result of an increasing contact velocity. The jet divergence also decreases with the increase in velocity. This in turn should result in more material being displaced from under the particle to the front of the crater during impact.

Experimental evidence and consideration of impact theory suggest that the high pressures and strain rates associated with solid particle erosion of the ceramic coatings result in the generation of significantly high localized temperatures in the surface of the coatings under high impact velocities. These temperatures are primarily limited by the absence of ideally adiabatic conditions [18]. Any heating of the coatings would lower the yield stress of the ceramic material and allow dislocation activity and a plastic response to particle erosion. However, the greater degree of irreversible deformation at the point of impact may lead to a greater driving force for lateral cracking during each isolated unloading cycle [2]. The extensive lateral cracking

seen at individual impact sites together with the evidence for plastic indentation as seen in Fig. 10g and h. Thus the possibility of plastic response to erosive impact due to increased surface temperatures may inadvertently lead to greater lateral spallation. The increase in plasticity at high velocities may concomitantly increase the erosion loss by the fracture of brittle materials since the greater degree of irreversible deformation will create an increase in the driving forces for lateral cracking during the unloading cycle.

Moreover, local thermal cycling may assist the formation and propagation of subsurface cracks and the general degradation of the target surface, thereby reducing the resistance to further impacts [19]. Greater erosion rates could thus be a consequence. On the other hand, the particles that strike the surface of a ductile material at an acute angle and at a velocity greater than the critical velocity needed for the penetration of the material's surface do remove some material, in a process similar to the cutting action of a machine tool. Fig. 10i displays the eroded surface of the uncoated substrate surface. At the impact location on the base material, the particle loses a fraction of its kinetic energy to the target material in the form of heat and energy for deformation of the surface. Very high levels of shear strain may be induced in the material at the impact location [20]. When the shear strain exceeds the elastic strain limit of the target material, the particle penetrates the surface of the material and ploughs along the surface, removing material as seen in Fig. 10i.

5.2. Effect of erodent particle impact angle on erosion rate

The effect of impact angle on the erosion rate of the base metal and ceramic coatings are displayed in Fig. 9. The mechanism by which material is removed from a surface upon erosion attack can be either ductile or brittle. In general, the ductile process is typified by maximum wastage at low impact angles. Most of metallic materials will erode by this mechanism. On the other hand for the brittle ceramic materials the erosion process is featured with maximum wastage at high impact angles, under which erosion occurs by cracking and chipping of surface material [5].

5.2.1. Erosion under low erodent particle impact angles

The worn surfaces of the ceramic coatings eroded under 30° impact angle are shown in Fig. 11a and b. The figure shows severe plastic shear deformation produced by the sliding action of erodent particles. There were evidences of rubbing, extrusion, ploughing and cutting actions of the impact particles. There is also evidence of brittle cracking, which finally led to the fragmentation of material. In the micrographs shown in Fig. 11a and b, one can see plastic shearing and rub bands which were produced by the erodent particles that rubbed the surface during erosion. An erosion pit was formed by cracking, which can be seen in the micrographs (Fig. 11a and b). Since, at the shallow impact angle of 30°, the contact of erodent particles with target surface contributed mainly to ploughing and very little to brittle cracking, the erosion at this impact angle is quite low, as seen in Fig. 11a and b.

The mechanisms of material removal of the ductile materials like the uncoated substrate are generally considered to be different at low and high impact angles. Nevertheless, it is suggested here that it involves deformation and fracture processes. It is considered that the highly deformed material formed into "chips" at low impact angles or crater "lips" formed at angles close to normal incidence [21]. Under low impact angles, the erodent particle will have the tendency to slide over the surface and as it slides, it will plough the material as observed in Fig. 11c. The subsequent sliding of the particle will remove the material from the surface. In other words, a certain portion of the volume swept out at low angles of incidence will simply be deformed and displaced in a ploughing action. Since the erodent particles are being in contact for long time on the surface during sliding, the wear rate is much high. Because of the different impingement angles of the sand particles, the eroded scars have different lengths and shapes (Fig. 11c). When the impact angle was increased to 60° for the ceramic coatings, the ploughing features changed, as seen in Fig. 11d and e. It is seen that a rub band was formed by plastic shear and the arrow points to a slip band. The material was lost here at the end of the rub band so that a pit is created. The smooth surface of the bottom of the pit indicates that the lamella was separated from the coating by lamellar cracking. Ceramic materials namely the chromias and aluminas can undergo plastic deformation even at room temperature during ploughing. Scratch tests exhibited plastic deformation on the groove surfaces accompanied by brittle failure of the groove edges [22].

It is evident that at shallow impingement angles, erosion damage is dominated by both splat ejection and plastic deformation of the lamellae. Further, in the plastically deformed areas, grooves or plough marks are often observed. The plastic grooves, in many instances, are similar to scratches produced on coated surfaces by a sharp and hard indenter and they tend to lie along the particle colliding direction. In the case of shallow angle eroded surfaces, shown in Fig. 11d and e, the dominant material removal mechanisms are splat ejection, which is caused by grain lamellar microcracking, and plastic deformation followed by smearing of the deformed materials. The low angle erosion of the uncoated substrate may perhaps be compared to abrasion. In the case of abrasive wear, three types of material removal mechanisms can occur [23]: cutting, wedge formation and ploughing. Only cutting and wedge formation lead to metal removal. It is suggested that there is a critical 'attack angle', below which the ploughing mechanism occurs. As attack angle is increased above this critical angle, a transition from ploughing to cutting occurs. It was proposed that a critical 'attack angle' for cutting also exists for erosive wear at low angles, with the formation of 'chips' only occurring at angles greater than this critical angle. It must be noted that this critical angle is not the impact angle of the impinging

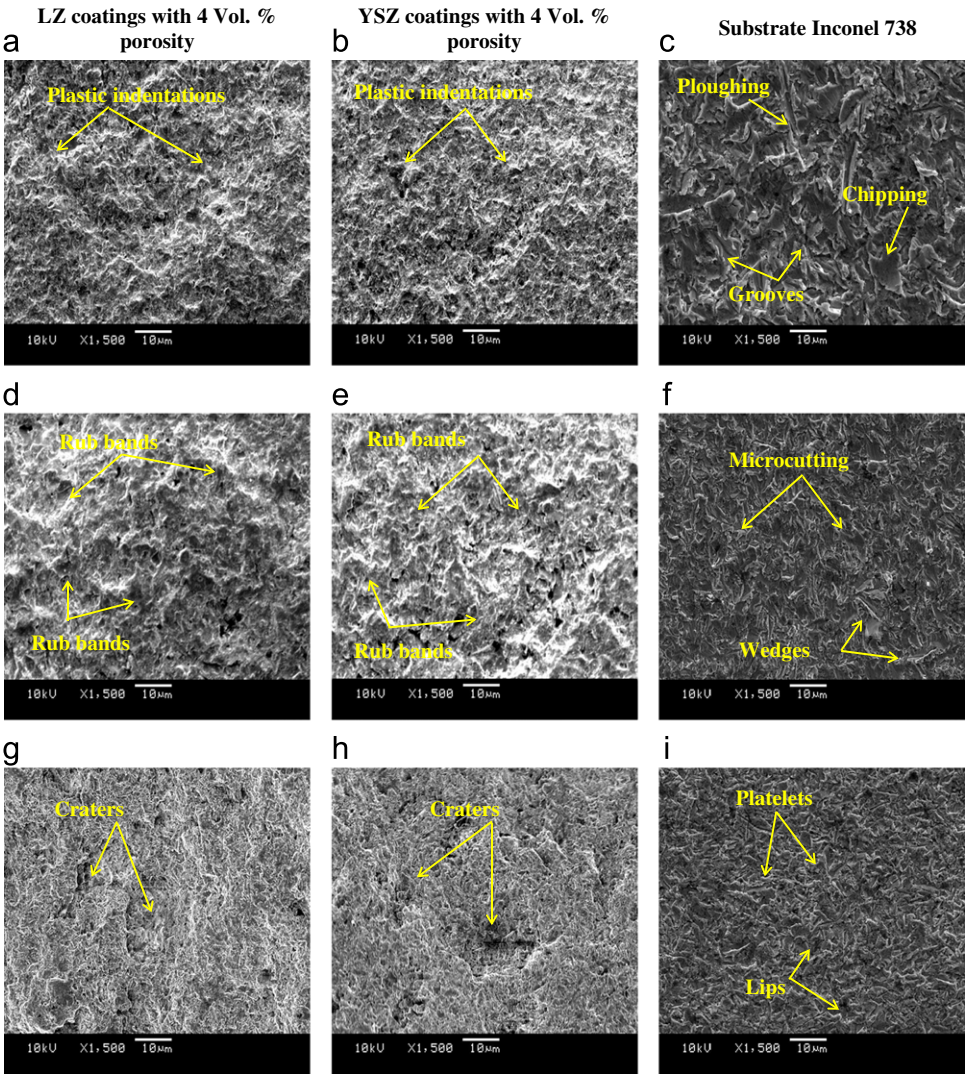

Fig. 11. Worn surfaces of coatings and substrate under different erodent particle impact angles. (a-c) Velocity of the erodent particle: 60 m/sec; Impact angle of the erodent particle: 30°; Erodent particle flux: 4 gpm; (d-f) Velocity of the erodent particle: 60 m/sec; Impact angle of the erodent particle: 60°; Erodent particle flux: 4 gpm; (g-h) Velocity of the erodent particle: 60 m/sec; Impact angle of the erodent particle: 90°;Erodent particle flux: 4 gpm.

particle, but rather the effective angle made by the leading face of the particle with the target surface. Cutting will only occur if the orientation of the particle at impact leads to an effective angle greater than the critical angle for cutting. In the case of ploughing, a wave of deformed material is pushed ahead of the sliding particle [24]. This creates a lip of material at the head of the impact crater as witnessed in Fig. 11f. It is usually considered that a number of impacting particles are necessary to remove the deformed lips. Erosion rate is considered to be dependent on the sub-surface shear strains resulting from the sliding particle. These will, in general, be greater for angular particles than spherical ones, owing to the higher attack angles presented by the former [25].

5.2.2. Erosion under high erodent particle impact angles

Zeng and Kim have divided the erosion mechanisms observed in brittle material erosion into six categories [26]: (1) conical, radial and lateral crack systems; (2) intergranular and transgranular cracking; (3) ring fracture, (4) microchipping; (5) plastic deformation and melting; and (6) mixed damage. Among the various erosion modes, conical crack and lateral crack together with plastic deformation have been claimed to dominate the brittle material removal process. The impact damage, which consists of surface spalling like the ones seen in the Fig. 11g and h, is attributable to the combined effect of lateral and radial crack formation in both surface and subsurface region and becomes the source of material degradation. On the other hand, the brittle process is featured with maximum wastage at high impact angles, under which erosion occurs by cracking and chipping of surface material. Under such kind of circumstances, a "Hertzian cone crack" will be initiated first due to the radial tensile stresses in the shallow surface layer around the contact area of the erodent particles [27]. Propagation of the initial

cracks occurs during subsequent attack by erodent particles, which may lead to the removal of ceramic material through a chipping process. Individual lamellae are cracked and then chipped before removal. Cracks are observed normal to the top surface lamellae terminating at their boundaries, which could be seen Fig. 11g and h. This suggests that inter-lamella bonding strength is influential in determining the erosion characteristics of thermal sprayed coatings. Coating porosity is often located along the lamella boundaries [28]. Not only will it influence the strength of the inter-lamella but may also initiate microcracking leading to the loss of lamellae and thus coating removal. The erosion involved material removal by breaking of the splat boundaries and their pull out along the grooves from the surface. The eroded surfaces shown in Fig. 11g and h reveal broken lamellae and fragmentation as well as large craters in the eroded zone. On the other hand, the surfaces eroded under 90° impact angle shown in Fig. 11g and h, it is evident that the damaged coating surface has become very rough with large undulations. The plastically deformed features were also found to become less pronounced.

For the uncoated substrate exposed under low attack angles, the cutting mechanism was highly prevalent. For high angles, the cavities with apparently plastically deformed edges are observed, suggesting the wear mechanism of platelet formation, which can be seen in Fig. 11i. During particle impact, the loss of material from an eroding surface may occur by a combined extrusion-forging mechanism. Platelets are initially extruded from shallow craters made by the impacting particle. Once formed, the platelets are forged into a strained condition, in which they are vulnerable to being knocked off the surface in one or several pieces [29]. From the appearance of the craters formed on the surface of the eroded material shown in Fig. 11i, it was observed that the surface material was forced to flow from the front and to the sides of the impacting particle, until the material was sufficiently strained so as to fracture, at which time the material loss occurred. Sheldon and Kanhere proposed the following sequence in the erosion process of metallic materials [30]:

During the incubation period of erosion, platelets are formed, initially without loss of material. Because of the high strain rates, adiabatic shear heating occurs in the surface region immediate to the impact site. Beneath the immediate surface region, a work-hardened zone forms, since the kinetic energy of the impacting particles is enough to result in a considerably greater force being imparted to the metal than is required to generate platelets at the surface. The hardened zone has discontinuities where softer material is open to the surface. Further, due to repeated impacts, the softer material from below the hardened layer is extruded out from these openings; a process they termed backward extrusion. The extruded material is then beaten into platelets by subsequent impacts, and wear results from the detachment of these platelets, which are evident in Fig. 11i.

In erosion, the surface is impacted not once but many times. The material element will undergo plastic flow with two significant consequences. First, residual stresses will develop and, second, the material may strain-harden thereby increasing its effective yield strength. Further impacts will subject the material to a combination of the impact stresses and the residual stresses developed previously. These residual stresses are essentially protective in the sense that they make subsequent yielding less likely, and this fact, together with any effects of strain-hardening, may be sufficient to ensure that after many impacts the steady state deformation of the material is entirely elastic. This is the process of 'shakedown' and the contact pressure limit below which it occurs is known as the 'elastic shakedown limit' [31].

When the metallic surface has been completely converted to platelets and craters (as seen in Fig. 11i) and the work-hardened zone has reached its stable hardness and thickness, steady state erosion begins. These cross section conditions of material will move down through the metal as erosion loss occurs. In the platelet mechanism of erosion there is localised sequential extrusion and forging of metal in a ductile manner, leading to removal of the micro segments thus formed. During plastic deformation, the normal component of the particle's kinetic energy is used to extrude-forge the material. A number of other mechanisms have been proposed for material removal (ductile materials) due to impingement at high angles [32]. These include brittle behaviour due to work hardening, fragmentation of the particles, low cycle fatigue, temperature effects due to high strain rates, shear band formation, delamination wear, and extrusion mechanisms.

5.3. Effect of erodent particle flux on erosion rate

The effect of particle flux on the erosion rate of the base metal and the ceramic coatings are displayed in Fig. 9. Particle flux is usually defined as the mass of particles striking the target surface per unit area per unit time. Adding even relatively small amounts of solid particles causes an increase in the gas turbulence and decreases the kinetic energy transmitted to the individual particle [33]. This turbulence attenuation increases the jet spreading rate and causes a faster decay of the gas mean centreline velocity, thereby reducing the erosion rate.

5.3.1. Erosion under low erodent particle flux conditions

When the particle flux at impact is reduced, the amount of erosion damage per unit mass of abrasive striking the target increases. The effect of particle–particle interactions within the injection venturi nozzle, particle-acceleration tube bore interactions and particle–particle interactions at the target surface can result in reduced erosion rates. Low fluxes are recommended to minimise these effects. Particle–particle interactions within the acceleration tube bore are thought negligible as the inter-particle spacings are always greater than ten times the particle diameter.

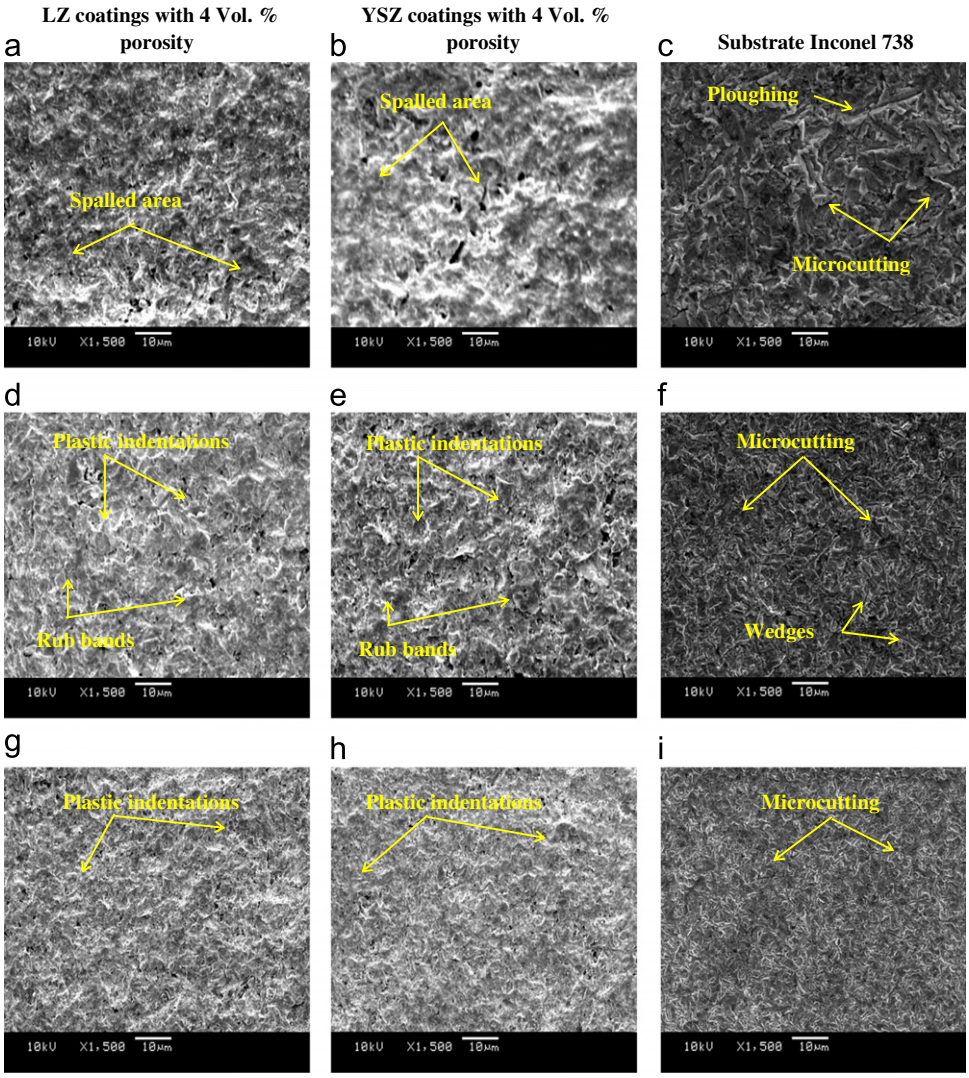

Fig. 12. Eroded surfaces of coatings and substrate under different erodent particle fluxes. (a-c) Velocity of the erodent particle: 60 m/sec; Impact angle of the erodent particle: 60°; Erodent particle flux: 2 gpm; (d-f) Velocity of the erodent particle: 60 m/sec; Impact angle of the erodent particle: 60°; Erodent particle flux: 4 gpm; (g-i) Velocity of the erodent particle: 60 m/sec; Impact angle of the erodent particle: 60°; Erodent particle flux: 6 gpm.

This flux effect has been described by Anand et al. by a first-order particle collision model in which a shielding of the target surface from the incident particles occurs [34]. When the erodent particle flux is low, the mean free path of the erodent particles is quite long and thus the probability of collision between the rebounding particles and the incident particles is very low. As the flux increases, the probability of collision increases exponentially and hence the erosion rate would be expected to decrease. The effect of particle flux on the erosion rate may also arise from the dependence of the incident particle velocity on the particle flux. According to the analysis by Anand et al., in airborne erosion apparatus, when the particle flux value is too high, hydrodynamic particle interactions occur in the nozzle and become more noticeable as the particle flux increases further [34]. At low erodent feed rate, the incident energy (impact energy) was higher (i.e., if there were no-interference effects). The effect of particle flux is evident on the eroded surface of the ceramic coatings and uncoated substrate as illustrated in the Fig. 12a–f. The Fig. 12a, b, d and e illustrate that the ceramic coatings underwent cracking, splat ejections along with lamellae spallation and propensity of cracking decreases with increasing particle flux values. The same kind of trend is also observed in case of the uncoated substrate, which possessed plough marks, cutting and wedge formations as seen in Fig. 12c and f.

5.3.2. *Erosion under high erodent particle flux conditions*

From the current solid particle erosion test, it is also apparent that the erosion rate is low at the highest particle concentrations compared to low flux conditions (Fig. 9). This can possibly be explained through a realisation that greater numbers of inter-particulate and particle-wall collisions will occur at a higher particle concentration. The effect of the collisions will be to slow down the

particles, as some of their kinetic energy will be lost in each collision. When the particle concentration decreases, the conveying velocity increases and there is an increased occurrence of erosion damage vice versa as could be witnessed in Fig. 12a–i. It is thought that the nature of the particle–particle interactions can be divided up into two parts [35]: It is believed that at low fluxes, the interactions that the particles are likely to experience from the time that they are introduced into the gas stream are particle–tube interactions which slow the particles down and account for the particle velocity being less than the gas velocity. This hypothesis suggests that as the number of particles in the tube increases, the more particle–tube interactions take place which should result in a drop in particle velocity as some of their kinetic energy will be lost in each collision as the flux increases. The fact that erosion damage is affected by particle concentration can be explained by the mechanism of "shielding" proposed by Andrews and Horsfield [36].

The mechanism of "shielding" is based upon the observation that inter particulate collisions cause more dispersed transfer of impinging energy to the eroding surface and as a result the quantity of erosion damage that occurs is decreased. With very high fluxes the number of particles which interact with the specimen surface are restricted by the shielding effect of particles rebounding from the surface and interacting with the incoming particles. It must be noted, however, that the flux density reaches a point where recoiling particles effectively shield the target from the very barrage of erodent sent to damage it. The aforementioned shielding effect lowers the erosion damage of the target surface as witnessed in Fig. 12g–i. It can be explained by momentum arguments that the number of particles striking the surface cannot be reduced by increasing the number of particle collisions but that incoming particles can be deflected so that they strike the surface at an angle that is sub-optimal for material removal. As long as the distance between the particles is large enough, a low number of collisions between particles occur. Most particles are able to strike the surface and leave the area before the next particle strikes the same area. With decreasing distance between particles, more and more rebound particles collide with incoming particles and slow them down and/or change their trajectories [37]. Both factors decrease the force or angle with which they strike the surface and, in some instances, prevent the incoming particles from even striking the target. It is observable in the Fig. 12g and h that the propensity of damage that is plastic indentations and rub bands are very low compared to the low flux conditions (Fig. 12a–f). It was also observed during the test that when the particle concentration increases, the divergence angle increases. In an air jet erosion tester, it is well known that the particles will spread out after leaving the acceleration tube. The resulting impact area on the targets will therefore be greater than the cross-sectional area of the acceleration tube leading to low erosion rates. This phenomenon is termed as particle plume (or particle jet) divergence [38].

The divergence obviously has an influence on both the particle impact angle and the surface flux. Divergence of the particle jet in the gas-blast tester may be attributed to aerodynamic coupling (between the particles and airstream carrying the particles), and interactions between particles and other particles or with the acceleration-tube-wall. The creation of a stagnation zone at the target surface also results in the "divergence" of gas stream lines. The Fig. 9 and Fig. 12g–i also confirm that inter-particulate collisions have an important effect on the jet divergence and reduction of erosion damage. It may be clearly seen that the divergence angle is greater at higher particle concentrations in the gas stream. The variable air-drag force and the effect of particle collisions also lead to a large divergence of the particle jet and consequently the low erosion rates [39].

5.4. Effect of coating porosity on erosion rate

Erosion is often regarded as many quasi-static single impacts. If pre-existing flaws are available, lateral cracking will occur under a low energy threshold value. The effect of porosity on erosion rate of coatings is displayed in Fig. 9. As expected, the erosion rate increases with the increase in the volume percentages of porosity. The plasma sprayed ceramic coating fails by propagation of cracks around splat boundaries and through the microcrack network, that are inherent as part of the plasma sprayed ceramic coating microstructure, and which provide a degree of strain tolerance under thermal cycling conditions [40]. This is not the case for a plasma sprayed ceramic coating under solid particle erosion, which when polished and then eroded, rapidly reverts back to a surface finish similar to, if not worse than, the as-sprayed values. For the erosion mechanism based on the residual tensile stress, fracture takes place with little increase in porosity relative to the large amount of homogeneous plastic deformation at fracture [41]. The influence of porosity on the erosion behaviour of materials depends on their microstructures and the erosion conditions. For ceramic coatings with varying percentages of porosity, three different types of erosion mechanisms with associated erosion rates were observed in the current investigation:

- The first type of morphology (eroded surfaces of coatings with a porosity value of 4 vol%) associated with low erosion rates is characterized by the presence of primary impact scars as the principal feature seen in Fig. 13a and b.
- The second type of morphology (eroded surfaces of coatings with a porosity value of 14 vol%) is associated with moderate levels of erosion. The erodent particles cause fractures to occur in the surface around the impact site as illustrated in Fig. 13c and d.
- The third type of morphology (eroded surfaces of coatings with porosity a value of 24 vol%) is characterized by the formation of tunnels on the surface and by relatively high rates of erosion. The surfaces with tunnels and gross fractured lamellae can be seen in Fig. 13e and f.

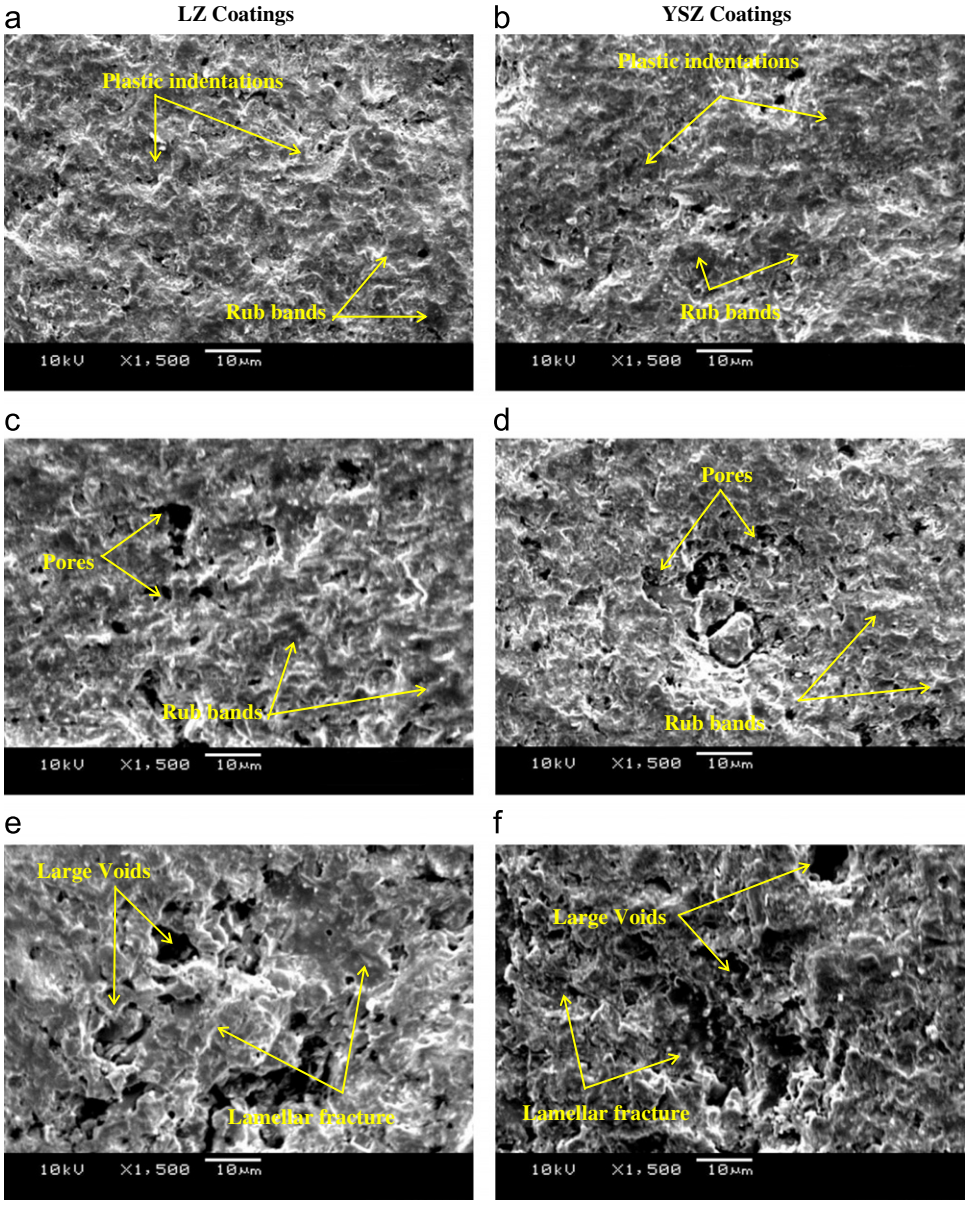

Fig. 13. Eroded surfaces of coatings with different vol% of porosity under an erodent particle velocity of 60 m/sec; erodent particle impact angle of 60° and an erodent particle flux of 4 gpm. (a-b) Porosity: 4 Vol. %; (c-d) Porosity: 14 Vol. %; (e-f) Porosity: 24 Vol. %.

5.4.1. Erosion of coatings having low volume percentage of porosity

The denser the coatings, the higher will be their hardness. In this case as the hardness increases the depth of penetration decreases so the erosion rate decreases. However, the hardness of the target is also used in determining the critical velocity for crack initiation. In this case as the hardness increases, the critical velocity to initiate cracking decreases. The stepwise erosion of the dense ceramic coated sample seen in Fig. 13a and b clearly shows that wear occurred by the accumulation of damage, fracture and removal of single splats of ceramic lamellae. The results show that wear occurs by progressive damage process that involves [42]:

- Accumulation of plastic strain in ceramic splats;
- Fracture and fragmentation of individual ceramic splats;
- Cracking between ceramic splats;

The splat ejection is the dominant material removal mechanism and significant amounts of plastically deformed material are also observed in the dense coatings as displayed in Fig. 13a and b. The lower porosity, coupled with the energy absorption capacity and the stronger bonding between ceramic splats, has made splat ejection more difficult. As a result, the repeated impact by particles causes plastic smearing of the splats before they are ejected. Thus, during the erosion test

cracks initiate at voids close to the surface. This suggests that the stresses are high enough to move into the plastic regime. This may be evidence that the sub-surface cracks are propagating under shear.

5.4.2. Erosion of coatings having high volume percentage of porosity

The presence of porosity can be very detrimental to the wear resistance of ceramic coatings. When an external force is applied to a ceramic coating, pores in the coating may act as stress raisers that facilitate crack initiation. Cracks could easily propagate by connecting pores with high stress concentration, leading to eventual surface failure of the coatings. The negative effect of porosity on the wear resistance is influenced by the pore size, shape and density [43]. If pre-existing flaws are available, lateral cracking may still occur below the energy threshold. In the case of dense coatings, which can be expected to have fewer flaws, the surface appears more uniformly damaged as revealed in Fig. 13a and b. So flaws play a role in the surface morphology. Lamellar interfaces in the plasma sprayed porous ceramic coatings do not bind perfectly with each other. These interfaces can be seen as pre-cracks in the coating. Under the impact of abrasives, the pre-crack tends to propagate along the bonded fraction of the lamellar interface. The propagation of the cracks through whole interface of the lamella exposed on the surface will lead to the spalling of the lamella [44]. As a result, the erosion of the coating occurs successively via the delamination of the lamella exposed on the surface one by one, which can be explained by the following sequence:

Initially, the deformation of coating took place at the inside of coating splats, forming small craters, indentations and striations which only resulted in slight erosion wastage. As the test proceeds, cracking and chipping of segments of coatings also occurred. These cracks appeared to be associated with areas, where there is a sharp transition in the structure and properties of the coatings such as at splat boundary phase and oxide interfaces often associated with porosity in the structure. Such chipping leads to loss of larger masses of material than ductile erosion and thus raises the erosion wastage, which could be seen in Fig. 13c and d. It is also clear from Fig. 13c and d that there were some lamellae cracked along the splat boundaries, and the fractured, loosened pieces on the eroded sample's surfaces. Cracking is thought to form first at splat boundaries during the impact of particles. Under the continual impacting of particles, the cracks were developed, and then fractured and loosened pieces were chipped off. Finally many voids and pits formed. A complicated relationship exists between the interlamellar bonding, the level of porosity and the amount of vertical and horizontal microcracking for plasma sprayed ceramic coatings. The porous morphology of coating causes the stress to spread discontinuously from the impact point. Fig. 13e and f also illustrate the material removal underneath the particle as it chips away the ceramic coatings. The particle penetrates into the coatings to roughly about 25 μm deep and begins to bounce back/upward.

It is evident that splat decohesion and brittle fracture of the splats by particle indentation-induced cracking were essential ingredients of the damage mechanisms. Linkage of the indentation cracks with pre-existing cracks in the coating could have aided the material removal process. The more porous coating may be associated with a modification in its mechanical properties, i.e., a decrease in the hardness. The pore sizes were also found to increase with the increase in volume percentages of porosity in the coatings [9]. Since average effects of pores are likely to be more consistent when larger areas are removed than when smaller small areas are removed, more consistent erosion can be observed. The results suggest the critical role of pores/cracks in the erosion mechanism. Unlike homogeneous materials, it appears that the porous microstructures play an important role in defining the erosion behaviour of ceramic coatings. The relative comparison of porosity contents of the coatings and respective erosion rates of coatings also suggests that the greater the porosity of the coating, the easier it is for the erodent particles to knock off pieces of exposed surface and the greater is the removal rate as seen in Fig. 13e and f. The porosity acts to reduce the mechanical strength, which further reduces the amount of energy required for the removal of parts of the surface. Similarly Westergard et al. [45] report that in erosion tests on plasma sprayed ceramic coatings entire splats or sub-splats were detached. The appearance of the eroded surfaces indicated that the cracks tended to follow a variety of weak sites to produce wear debris. Sub-surface crack propagation along regions of microstructural weakness thus appears to play an important role in the erosion resistance of plasma sprayed ceramic coatings.

5.5. Reasons behind the differences in the erosion behaviour of the YSZ and LZ coatings

It is well known that the amount of damage in solid particles impact erosion largely depends on the ratio of particle hardness to the specimen hardness. The hardness of the corundum erodent was 2375 $HV_{0.3}$. It was noticed that with the increasing ratio of particle hardness to target hardness (H_p/H_t) ratio the erosion rate increases [46]. In a similar manner to abrasive wear, it has been shown that the erosion rate reduces when $H_p/H_t < 1$. Below this figure, erosion mechanisms like microcracking and microchipping mechanisms are observed. For brittle materials where $H_p/H_t > 1$ material is removed by the indentation induced fracture. In general, if the hardness of an abrasive exceeds that of ceramic coating, the following processes take place [47]:

Penetration of abrasive into the coating, microcutting, and failure of splats resulting in the detachment of small chips. Since the erosion of brittle lamellae is primarily via a mechanism involving the initiation and propagation of microcracks, one expects that the fracture toughness of the

Table 9
Comparative values of H_p/H_t ratios and H^3/E^2 ratios of LZ and YSZ coatings.

Material	Microhardness (H) ($HV_{0.3}$)	Microhardness (H) (GPa)	Young's modulus (E) (GPa)	H_p/H_t	H^3/E^2
YSZ	1149 (coating with 4 vol% porosity)	11.27	220 (Sintered)	2.07	0.031
LZ	1184 (coating with 4 vol% porosity)	11.61	175 (Sintered)	2.00	0.051
Corundum (Sintered)	2375	23.29	217	–	–

H_p: Microhardness of the erodent particle; H_t: Microhardness of the target.

material will affect the erosion rate. Fracture toughness is usually assumed to be one of the indicators of the wear resistance of these types of materials in environments where brittle fracture is the predominant mode of material removal [48]. This fact is due to the higher energy needed to initiate and propagate cracks in the target material when there is an increase in the fracture toughness. For plasma sprayed ceramic coatings, better correlations were found between the hardness of the wearing material and the modes of erosion, where plastic deformation was a major mechanism. The erosion rate increased sharply as the coating hardness decreased. This increase is due to a combination of inter-lamellar porosity and poor intersplat bonding in these coatings, as neither factor by itself can account for it. Erosion of plasma sprayed ceramic coatings by hard particles usually involves both plastic flow and brittle fracture at the same time. The effect of fracture toughness on the wear resistance of brittle materials is usually related to the hardness [49]. The wear of brittle materials based on mechanical properties such as hardness, elastic modulus and fracture toughness, which have proven inadequate for engineering ceramics, are also unsuitable for predicting the wear of the plasma sprayed ceramic coatings [50].

In this study of the interrelation of the erosion behaviour of plasma sprayed ceramic coatings to their microstructural and micromechanical characteristics, the best correlations were found between the material hardness, the level of porosity and the erosion rate. From the Table 1 it could be inferred that the LZ coating possesses high hardness compared to YSZ coatings. The young's modulus values (175 GPa for LZ and 220 GPa for YSZ) and the fracture toughness values (LZ: 1.4 $MPa/m^{1/2}$ and YSZ: 1.8 $MPa/m^{1/2}$) of the LZ ceramic are lower than that of the YSZ [51]. The calculated H_p/H_t and H^3/E^2 ratios for the coatings are shown in Table 9. Due to the specific mechanical properties of the LZ ceramic such as low H_p/H_t ratio value, very high H (Hardness), low E (Young's modulus) and consequently high-H^3/E^2 ratio, such coatings are good candidates for protection against solid particle erosion compared to YSZ coatings. It can be summarised that with increasing severity of erosion conditions, the erosion rate showed stronger dependence on H_p/H_t. The transition in wear rates from mild to moderate to severe erosion conditions was associated with change in erosion mechanism under these conditions with increase in the porosity of the coatings. Furthermore, the crystal

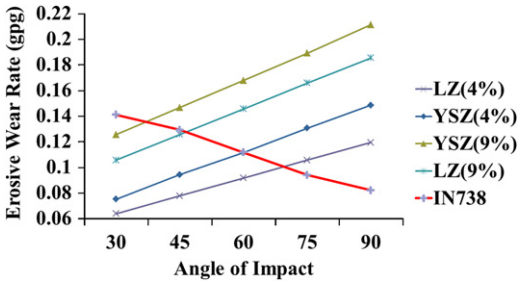

Fig. 14. Comparison graph depicting the erosion resistance of coatings with respect to different volume percentages of porosity under an erodent particle flux of 2 gpm and an erodent particle velocity of 100 m/s.

structure can influence the erosion rate. Stacking fault energy and dislocation cell formation are thought to be factors which influence erosion as a function of crystal structure. XRD analyses of the eroded specimens were performed and it was found that there was no phase transformation in the coatings and the patterns were the same as the as coated specimens. Shipway and Hutchings [52] identified the following as being important target material characteristics to consider in solid particle erosion: hardness, strain rate sensitivity, grain orientation, grain size effects, thermal parameters and toughness. Of these, hardness has been the most extensively studied. It has been found when comparing different pure materials that harder materials generally erode less.

5.6. Comparison of erosion resistance of base metal and coatings

To directly compare the erosion resistance of coatings against base metal, a graph shown in Fig. 14 was drawn, having in horizontal axis are values, which represent the impact angles. The vertical axis represents the erosion rate. The plotted points were derived from the regression equations by keeping the parameters namely the feed rate and the velocity constant at 2 gpm and 100 m/s, respectively, which were found to be aggressive erosion conditions. The graph was plotted to find out up to how much volume percentage of porosity the coatings could offer better erosion resistance than the base metal. From the graph (Fig. 14) it was found that up to 4% volume of porosity the coatings will offer better wear resistance than the base metal under oblique impact (up to

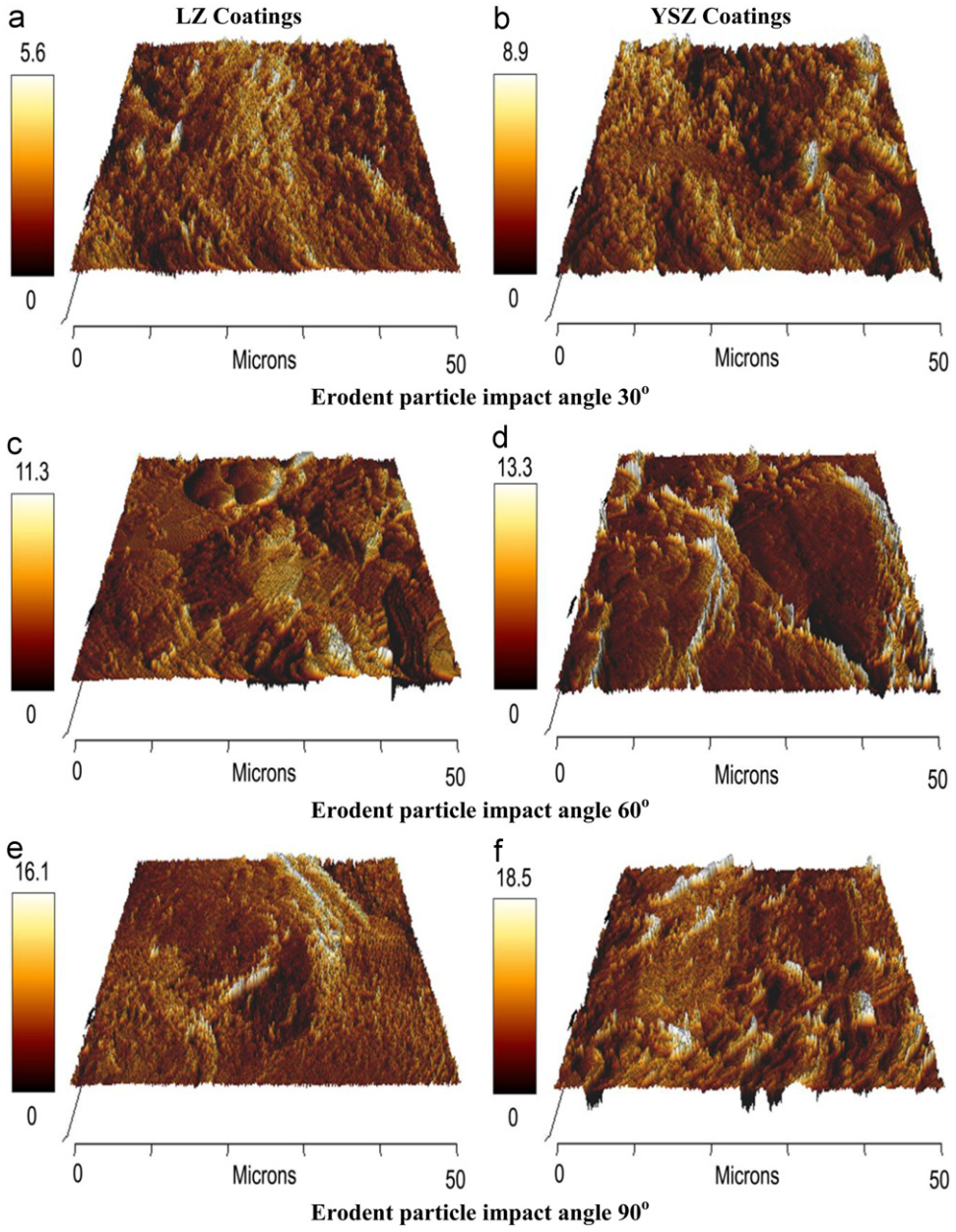

Fig. 15. AFM analysis of eroded surfaces of coatings having 4 vol% of porosity exposed under different erodent particle impact angles with 2 gpm of erodent particle flux and an erodent particle velocity of 100 m/s.

60°). An AFM analysis was carried out on the centre of the eroded pits of coatings containing 4 vol% of porosity exposed under different impact angles with 2 gpm of particle flux and a velocity of 100 m/s. From the analysis it was inferred that the peak to valley rough increases with increase in the impact angle as witnessed in Fig. 15. From the same figure one could see that the roughness values of the eroded LZ coatings are comparatively lower than that of the roughness values of the eroded YSZ coatings. The high wear resistance of the LZ coating compared to YSZ coating is due to its high hardness and low young's modulus. The aforementioned properties lowered the H_p/H_t ratio and increased the H^3/E^2 ratio of LZ coatings and in turn minimising the erosion rate of the LZ coating compared to the YSZ coats.

6. Conclusions

- In the present investigation the effects of solid particle erosion parameters namely the vol% of porosity present the coatings, the velocity of the erodent particle, the angle of impact of the erodent particle and the erodent particle flux were studied using response surface methodology (RSM).
- Empirical relationships were established using RSM to predict the erosion rate of the uncoated and coated coupons.
- Out of the four parameters considered, the vol% of porosity present in coatings was the most predominant factor affecting the erosion rate of the coatings. The

factors (parameters) namely the impact velocity of the erodent particle, angle of impact of the erodent particle and the erodent particle flux can be considered, respectively, as the next most important parameters influencing the erosion rate.

- The LZ coatings, indeed exhibit a good erosion resistance, whereas the YSZ coatings comparatively underwent higher erosive wear loss. The erosion resistance of the uncoated substrate was at its best, compared to coatings under perpendicular (normal angle) impact conditions.
- Both the coatings performed better than the substrate when they had 4 vol% porosity particularly below an impact angle of 60°. When the porosity of the coatings was above 4 vol% the erosion resistance was poorer than that of the Inconel 738 substrate.
- Due to the specific mechanical properties of the LZ ceramic such as low H_p/H_t ratio value, very high H (Hardness), low E (Young's modulus) and consequently high-H^3/E^2 ratio, such coatings are good candidates for protection against solid particle erosion compared to YSZ coatings.
- It should be emphasised that the range selected for parameters, the results and the conclusions refer specifically to the air jet erosion test setup employed in the present study. However, the illustrated approach and the methodology of the response surfaces are common.

Acknowledgements

The corresponding author wishes to express his sincere thanks to the Department of Science and Technology (DST), Govt. of India, New Delhi for the fellowship and financial support extended to carry out this investigation through the sponsored fast track scheme for young scientists—R&D project No. SR/FT/ETA-01/2009.

References

[1] R.J.L. Steenbakker, R.G. Wellman, J.R. Nicholls, Erosion of gadolinia doped EB-PVD TBCs., Surface and Coating Technology 201 (2006) 2140–2146.
[2] J.R. Nicholls, M.J. Deakin, D.S. Rickerby, A comparison between the erosion behaviour of thermal spray and electron beam physical vapour deposition thermal barrier coatings, Wear 235 (1999) 352–361.
[3] B.Z. Janos, E. Lugscheider, P. Remer, Effect of thermal aging on the erosion resistance of air plasma sprayed zirconia thermal barrier coating, Surface and Coating Technology 113 (1999) 278–285.
[4] Jiing-Herng Pi-Chuen Tsai, Chi-Lung Lee, Chang, Improving the erosion resistance of plasma-sprayed zirconia thermal barrier coatings by laser glazing, Surface and Coating Technology 202 (2007) 719–724.
[5] F. Cernuschi, L. Lorenzoni, S. Capelli, C. Guardamagna, M. Karger, R. Vaßen, K. Von Niessen, N. Markocsan, J. Menuey, Carlo Giolli, Solid particle erosion of thermal spray and physical vapour deposition thermal barrier coatings, Wear 271 (2011) 2909–2918.
[6] G.Levi Carlos, Emerging materials and processes for thermal barrier systems, Current Opinion in Solid State & Materials Science 8 (2004) 77–91.
[7] X.Q. Cao, R. Vassen, D. Stoever, Ceramic materials for thermal barrier coatings, Journal of European Ceramic Society 24 (2004) 1–10.
[8] D. Grove, T. Davis, Engineering Quality and Experimental Design, Longman Scientific and Technical, Harlow, U.K., 1992.
[9] C.S. Ramachandran, V. Balasubramanian, P.V. Ananthapadmanabhan, Synthesis, spheroidization and spray deposition of lanthanum zirconate using thermal plasma process, Surface and Coating Technology 206 (2012) 3017–3035.
[10] C.S. Ramachandran, V. Balasubramanian, P.V. Ananthapadmanabhan, On resultant properties of atmospheric plasma sprayed yttria stabilised zirconia coating deposits: designed experimental and characterisation analysis, Surface Engineering 27 (2011) 217–229.
[11] A.I. Khuri, J.A Cornell, Response Surfaces: Design and Analysis, Marcel Dekker Ltd., New York, U.S.A., 1996.
[12] K.Y. Benyounis, A.G. Olabi, Optimization of different welding processes using statistical and numerical approaches—a reference guide, Advanced Engineering Software 39 (2008) 483–496.
[13] S. Kumar, P. Kumar, H.S. Shan, Effect of evaporative pattern casting process parameters on the surface roughness of Al–7% Si alloy castings, Journal of Material Processing Technology 182 (2007) 615–623.
[14] Stat Ease Inc., Minneapolis, U.S.A, 2009.
[15] T. Denga, M.S. Bingley, M.S.A. Bradley, S.R. De Silva, A comparison of the gas-blast and centrifugal-accelerator erosion testers: the influence of particle dynamics, Wear 265 (2008) 945–955.
[16] R.A. Doyle, A. Ball, On thermo mechanical effects during solid particle erosion, Wear 87 (1991) 87–95.
[17] M. Suckling, C. Allen, Critical variables in high temperature erosive wear, Wear 204 (1997) 528–536.
[18] B.A. Lindsley, A.R. Marder, The effect of velocity on the solid particle erosion rate of alloys, Wear 229 (1999) 510–516.
[19] Henk Wensink, C Miko, A Elwenspoek, closer look at the ductile–brittle transition in solid particle erosion, Wear 253 (2002) 1035–1043.
[20] B.F. Levin, J.N. Dupont, A.R. Marder, Weld overlay coatings for erosion control, Wear 183 (1995) 810–820.
[21] J.G. Mbabazi, T.J. Sheer, R. Shandu, A model to predict erosion on mild steel surfaces impacted by boiler fly ash particles, Wear 257 (2004) 612–624.
[22] Y. Xie, H.M. Hawthorne, The damage mechanisms of several plasma-sprayed ceramic coatings in controlled scratching, Wear 235 (1999) 293–305.
[23] D.J. OFlynn, M.S. Bingley, M.S.A. Bradley, A.J. Burnett, A model to predict the solid particle erosion rate of metals and its assessment using heat-treated steels, Wear 248 (2001) 162–177.
[24] M. Danian Chen, S.T.S. Sarumi, Al Hassani, Computational mean particle erosion model, Wear 214 (1998) 64–73.
[25] Girish R Desale, Bhupendra K Gandhi, S.C. Jain, Effect of erodent properties on erosion wear of ductile type materials, Wear 261 (2006) 914–921.
[26] J. Zeng, T.J. Kim, An erosion model of polycrystalline ceramics in abrasive water jet cutting, Wear 193 (1996) 207–217.
[27] R.G. Wellman, J.R. Nicholls, High temperature erosion–oxidation mechanisms, maps and models, Wear 256 (2004) 907–917.
[28] Y. Wang, M. Yan, The effect of CeO_2 on the erosion and abrasive wear of thermal sprayed FeAl intermetallic alloy coatings, Wear 261 (2006) 1201–1207.
[29] G. Sundararajan, Comprehensive model for the solid particle erosion of ductile materials, Wear 149 (1991) 111–127.
[30] G.I. Sheldon, A. Kanhere, An investigation of impingement erosion using single particles, Wear 21 (1972) 195–209.
[31] S. Kulkarni, G.T. Hahn, C.A. Rubin, V. Bhargava, Elasto-plastic finite element analysis of three-dimensional pure rolling contact above the shakedown limit, Transactions ASMEE Journal of Applied Mechanics 58 (1991) 347–353.
[32] S. Chinnadurai, S. Bahadur, High-temperature erosion of Haynes and Waspaloy: effect of temperature and erosion mechanisms, Wear 187 (1995) 299–305.

[33] A.J. Burnett, S.R. De Silva, A.R. Reed, Comparisons between 'sand blast'' and 'centripetal effect accelerator' type erosion testers, Wear 187 (1995) 168–178.
[34] K. Anand, S.K. Hovis, H. Conrad, R.O. Scattergood, Flux effects in solid particle erosion, Wear 118 (1987) 243–257.
[35] Qianpu Wang, Morten C. Melaaen, T.Sunil De Silva, Guifang Tong, Experimental and computational studies of gas-particle flow in a sand-blast type of erosion tester, Powder Technology 160 (2005) 93–102.
[36] D.R. Andrews, N. Horsfield, Particle collisions in the vicinity of an eroding surface, Journal of Physics D Applied Physics 16 (1983) 525–538.
[37] S.M. Walley, JE. Field, The contribution of the Cavendish Laboratory to the understanding of solid particle erosion mechanisms, Wear 258 (2005) 552–566.
[38] Mark S. Tong Deng, Mike S.A.Bradley Bingley, Understanding particle dynamics in erosion testers—a review of influences of particle movement on erosion test conditions, Wear 267 (2009) 2132–2140.
[39] P.H. Shipway, The effect of plume divergence on the spatial distribution and magnitude of wear in gas-blast erosion, Wear 205 (1997) 169–177.
[40] W. Tabakoff, Investigation of coatings at high temperature for use in turbomachinery, Surface and Coating Technology 940 (1989) 97–115.
[41] L.C. Erickson, H.M. Hawthorne, T. Troczynski, Correlations between microstructural parameters, micromechanical properties and wear resistance of plasma sprayed ceramic coatings, Wear 250 (2001) 569–575.
[42] M.G. Gee, C. Phatak, R. Darling, Determination of wear mechanisms by stepwise erosion and stereological analysis, Wear 258 (2005) 412–425.
[43] Q. Chen, D.Y. Li, Bruce Cook, Is porosity always detrimental to the wear resistance of materials—a computational study on the effect of porosity on erosive wear of TiC/Cu composites, Wear 267 (2009) 1153–1159.
[44] J. Barber, B.G. Mellor, R.J.K. Wood, The development of sub-surface damage during high energy solid particle erosion of a thermally sprayed WC–Co–Cr coating, Wear 259 (2005) 125–134.
[45] R. Westergard, N. Axen, U. Wiklund, S. Hogmark, An evaluation of plasma sprayed ceramic coatings by erosion, abrasion and bend testing, Wear 246 (2000) 12–19.
[46] Irina Hussainova, Microstructure and erosive wear in ceramic-based composites, Wear 258 (2005) 357–365.
[47] C. Dogan, J. Hawk, Role of composition and microstructure in the abrasive wear of high-alumina ceramics, Wear 229 (1999) 1050–1058.
[48] E. Evans, Charles, fracture toughness determinations by indentation, Journal of American Ceramic Socirty 62 (1979) 371–382.
[49] R.G. Wellman, M.J. Deakin, J.R. Nicholls, The effect of TBC morphology on the erosion rate of EB PVD TBCs, Wear 258 (2005) 349–356.
[50] L.C. Erickson, R. Westergård, U. Wiklund, N. Axén, H.M. Hawthorne, S. Hogmark, Cohesion in plasma sprayed coatings—a comparison between evaluation methods, Wear 214 (1998) 30–37.
[51] R. Vassen, X. Cao, F. Tietz, D. Basu, D. Stover, Zirconates as new materials for thermal barrier coatings, Journal of American Ceramic Society 83 (2000) 2023–2028.
[52] P.H. Shipway, I.M. Hutchings, The role of particle properties in the erosion of brittle materials, Wear 193 (1996) 105–113.